

Technical Report

Analysis of Three Body Final States in Flight

Jörg Lüdemann, Ruhr-Universität Bochum

Bochum. October 30th, 1995

Abstract: Antiproton-proton annihilation into three neutral pseudoscalar mesons with incident antiproton beam momenta of 600 MeV/c and 1940 MeV/c has been studied with the Crystal Barrel spectrometer at CERN. The data were taken with a trigger on antiproton interaction, zero charged tracks and calorimeter energy sum in order to acquire only all neutral final states.

The mass range for the detection of intermediate states is enlarged up to $2.2 \text{ GeV}/c^2$ as compared to $1.7 \text{ GeV}/c^2$ in annihilation at rest. Whereas the reaction at rest proceeds via relative S and P states, with increasing beam momentum higher spins contribute.

For the first time the production of the $f_0(1500)$ in reactions in flight is observed. Besides weak signals in the Dalitz plots of an isoscalar state at a mass of approximately $1.85 \text{ GeV}/c^2$ and an isovector state at $1.9 \text{ GeV}/c^2$ two $J^{PC} = 2^{++}$ states decaying into $\pi^0\pi^0$ ($M = 1640 \text{ MeV}/c^2$, $\Gamma = 169 \text{ MeV}/c^2$) and $\pi^0\eta$ ($M = 1650 \text{ MeV}/c^2$, $\Gamma = 260 \text{ MeV}/c^2$) respectively have been observed. In the $\eta\eta$ invariant mass region above $2 \text{ GeV}/c^2$ a heavy resonance is required to describe the data.

According to predictions from lattice QCD this heavy object might be the lightest tensor glueball. The other four states are good candidates for the first and second radial excitations of the non-strange tensor mesons.

Content

Content	2
1. Selection and reconstruction	4
1.1. Reconstruction of the photons	4
1.2. Preselection	4
1.3. Constraint fit	5
1.4. Errors of the measured quantities	6
1.5. Selection of final states	7
1.6. Results of the selection of the 6γ final states at 1.94 GeV/c	8
1.7. Selection of the final state $3\pi^0$ at $p_{\bar{p}} = 600$ MeV/c	9
2. Presentation of the data	12
2.1. Kinematics of three body reactions in flight	12
2.2. Two-photon invariant masses	12
2.3. Spectra of selected final states	13
2.3.1. $\pi^0\pi^0\pi^0$ at 1940 MeV/c	13
2.3.2. $\pi^0\pi^0\eta$ at 1940 MeV/c	15
2.3.3. $\pi^0\eta\eta$ at 1940 MeV/c	15
2.3.4. $\eta\eta\eta$ at 1940 MeV/c	16
2.3.5. $\pi^0\pi^0\pi^0$ at 600 MeV/c	16
3. Partial wave analysis	20
3.1. Isobar model	21
3.1.1. Helicity formalism	22
3.1.2. Parameters in the helicity formalism	23
3.1.3. Canonical description of angular distributions	25
3.1.4. Parameters in the canonical approach	25
3.2. Likelihood fit	26
4. Results of the analysis	28
4.1. The reaction $p\bar{p} \rightarrow \pi^0\pi^0\pi^0$ at 600 MeV/c	28
4.2. The reaction $p\bar{p} \rightarrow \pi^0\eta\eta$ at 1940 MeV/c	31
A Formulae for kinematic quantities	38
B Formulae used in the best fits	40
B.1. Weight function for the reaction $p\bar{p} \rightarrow \pi^0\pi^0\pi^0$ at 600 MeV/c	40
B.2. Weight function for the reaction $p\bar{p} \rightarrow \pi^0\eta\eta$ at 1940 MeV/c	41
Bibliography	42

1. Selection and reconstruction

The data used with an incident antiproton beam momentum of 1.94 GeV/ c were recorded in July 1992 and August 1994, the ones with 0.6 GeV/ c beam momentum in April 1993. All 600 MeV/ c data and almost all 1940 MeV/ c data were taken with a zero-prong trigger requiring a reacting antiproton in the target defined by the entrance counters and no signal from the veto counters downstream behind the target. Furthermore neither hits in the PWCs nor in the inner most three layers of the JDC were demanded. Additionally, a lower threshold in the fast FERA energy sum (Tony's box) was set.

For the studied reactions only π^0 's and η 's decaying into two photons were considered. The final states $\pi^0\pi^0\pi^0$, $\pi^0\pi^0\eta$, $\pi^0\eta\eta$ and $\eta\eta\eta$ were reconstructed from six measured photon hits in the electromagnetic calorimeter.

For the reconstruction standard CB software was applied to the data: CBOFF 1.27/05[4], LOCATER 1.97/04[5], BCTRAK 2.03/00[6] and GTRACK 1.34/01[7]. These libraries were interfaced with CBoff++[8].

1.1. Reconstruction of the photons

The standard cut of 1 MeV as minimum energy deposit per crystal was applied during reconstruction of the photons. Clusters and PEDs with energy deposits less than 20 MeV were rejected.

The energies were corrected using the updated energy correction function[9]. In order to obtain an improved spatial resolution the 'Rainer Glantz' ped smoothing (PDRG flag set in BCTRAK) was applied[11]. The reconstructed values for ϑ are corrected by about 10 mrad for PEDs with central crystal type 11-13.

All Monte Carlo studies were done using CBGEANT 4.06/07[10] basing on the CERN software package GEANT 3.15/90[12]. Efficiencies and acceptances were estimated with the help of Monte Carlo technique.

1.2. Preselection

The cuts of the preselection are:

1. **no charged track** from LOCATER
2. **exactly six photons** from BCTRAK. Only PEDs with energy deposits greater than 20 MeV are considered as photons.

The left spectrum in figure 1.1 shows the multiplicity of charged tracks in the all neutral triggered data. The multiplicity of photons after rejection of charged events is shown in the right spectrum.

A preselection cut on total energy and momentum of the events was not applied. Complete events are more effectively recognized and selected by means of a constraint fit. In figure 1.2 the distribution of total energy versus total momentum of pure neutral events is shown. Due to the hermiticity of the detector and the required minimum energy deposited in the calorimeter during data taking most of the events fulfill already energy momentum balance within the expected errors of measurement.

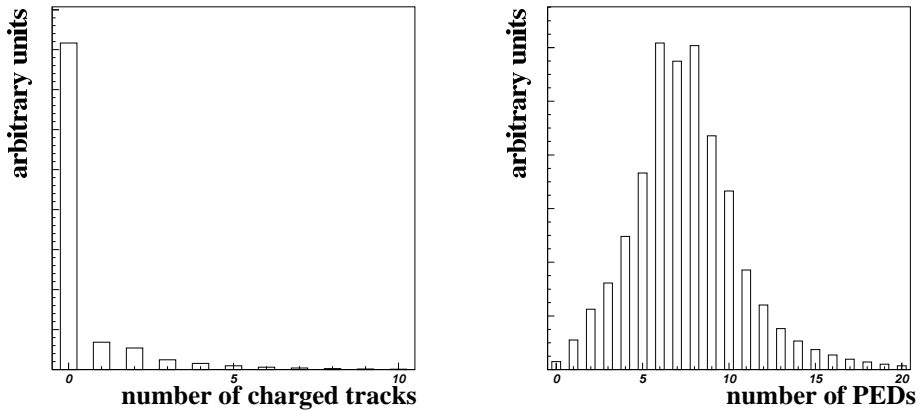


Figure 1.1: Multiplicities before preselection. The left spectrum shows the multiplicity of charged tracks found offline. On the right hand side the multiplicity of PEDs after rejecting charged events is shown.

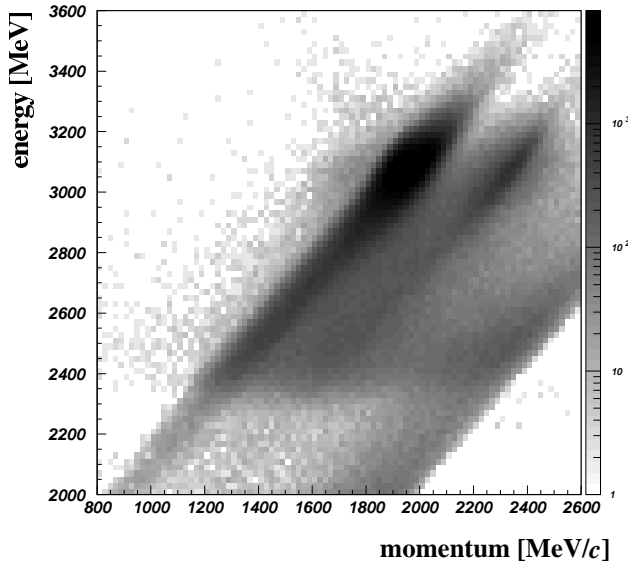


Figure 1.2: Total energy versus total momentum. The number of entries in each cell is drawn in logarithmic scale to visualize weak structures. Besides the strong enhancement where fully reconstructed events are expected (momentum = 1940 MeV/c, energy = 3093 MeV) regions can be identified where one photon could not be seen (diagonal bands). The reoccurrence of a similar structure at higher momenta is resulting from reactions in the veto counter, which did not work with 100% efficiency. These events were recorded but the photon momenta were not calculated correctly.

Cuts typically applied in analyses of at rest data were carefully studied. The rejection of events with PEDs in the outermost crystals (crystal type 13) is fatal when analyzing reactions in flight. Due to the expected leakage losses at the edge of the calorimeter this cut appears to be reasonable, however it reduces the covered solid angle in the c.m. system drastically. Actually a large fraction of those events are of high quality and badly measured events are rejected later on by the constraint fit. Similarly a cut vetoing events flagged as pile-up events was not applied. Real pile-up events are rejected by the further selection and many good events were flagged as pile-up. Also no split-off recognition algorithm was applied to the data, as the background of five photon events with one additional electromagnetic split-off could be well estimated and suppressed more efficiently by other means.

1.3. Constraint fit

The simultaneous measurement of all particles in the final state and the complete determination of their kinematics allows a constraint fit to improve the data quality. Moreover such a constraint fit

yields the possibility to test hypotheses such that events can be classified. Another output of an successfully converged kinematical fit are four-vectors which fulfill the imposed constraints. As this method is not implemented correctly for purely neutral final states in flight into CBKFIT, a self-made code was used. This code fits all measured kinematical quantities of the six photons (ϑ , φ , \sqrt{E}) and allows for a completely freely adjustable z-coordinate of the primary reaction vertex. The formulas involved can be found e.g. in [13]. CBKFIT (CASE.EQ.6) has not been used because there the vertex's position is calculated by newton iteration from the photon z-momenta and then treated in the fit as a measured quantity with a fixed error. This treatment gives rise to large covariances among most of the involved quantities which is not taken into account in CBKFIT, where all off-diagonal elements of the covariance matrix are fixed to zero and also an evaluation of the true error of measurement of the vertex position by means of error propagation is not implemented. It turns out that the actually used method in this analysis is not only the correct mathematical formulation but also improves the selection and reconstruction chain with respect to efficiency, invariant mass resolution and separation of final states by confidence levels.

Kinematical fits were applied testing the following hypotheses:

1. $\bar{p}p \rightarrow 6\gamma$, 3 constraints
2. $\bar{p}p \rightarrow \pi^0\pi^0\gamma\gamma$, 5 constraints
3. $\bar{p}p \rightarrow \pi^0\pi^0\pi^0$, 6 constraints
4. $\bar{p}p \rightarrow \pi^0\pi^0\eta$, 6 constraints
5. $\bar{p}p \rightarrow \pi^0\eta\eta$, 6 constraints
6. $\bar{p}p \rightarrow \eta\eta\eta$, 6 constraints

For the hypotheses 2, 4 and 5 45 permutations of the sequence of the six photons were tried, for the third hypothesis 90 permutations and for the hypotheses 3 and 6 15 permutations each. In order to minimize CPU time the permutations of interest are preselected by windows in the invariant mass. The boundaries of these were chosen large enough not to lose any event: 70-200 MeV/ c^2 for pions and 450-650 MeV/ c^2 for eta-mesons.

1.4. Errors of the measured quantities

The prerequisite for the application of a constraint fit is the knowledge of the errors of measurement. The error in \sqrt{E} is estimated to be

$$\sigma(\sqrt{E})/E = 2.8\% \sqrt{E}, E \text{ in GeV.} \quad (1.1)$$

A lower limit of $\sigma(\sqrt{E}) > 0.35 \text{ MeV}^{1/2}$ is superimposed. The errors for φ and ϑ were determined in [11] for energies up to 1 GeV for crystal types 1 to 12 and parametrized by

$$p_1 + p_2 \sqrt{E} + p_3 \ln(E), E \text{ in MeV.} \quad (1.2)$$

The parameters p_1 , p_2 and p_3 were determined separately for the cases of one or several PEDs per cluster and separately for edge and central crystals. A Monte Carlo study showed that this parametrization cannot be used for photon energies higher than 1 GeV which frequently occur in in flight reactions. Therefore the errors as calculated by BCTRACK were not used for φ and ϑ . They were overwritten by values based on a study of the reconstruction of Monte Carlo events generated with 1.94 GeV/ c antiproton momentum (tab. 1.1). These new estimates had to be scaled for the kinematical fit (tab. 1.2) in order to compensate systematical difficulties, e.g. the non-gaussian distribution of the error of energies. These scaling factors were determined separately for measured data and Monte-Carlo events by adjusting the widths of the pull distributions resulting from the constraint fit. The good estimate of the errors shows up in a flat distribution of the confidence level for events which are fitted with the correct hypothesis (fig.1.3).

	PED/Cluster	Type	σ in mrad (E in GeV)	F	E_0 in GeV	
φ	1	1-10	$27.26 - 35.68 E + 30.38 E^2 - 9.28 E^3$		1.4	
		11-13	$53.89 - 65.15 E + 48.15 E^2 - 12.8 E^3$	1.3	1.6	
	2	1-10	hi	$24.36 - 23.92 E + 17.79 E^2 - 4.99 E^3$		1.5
			lo	$= \text{hi} / 0.93$		
		11-13	hi	$47.98 - 48.3 E + 35.85 E^2 - 9.76 E^3$	1.25	1.8
			lo	$= \text{hi} / 0.88$		
ϑ	1	1-10	$27.3 - 49.69 E + 67.16 E^2 - 43 E^3 + 10 E^4$		1.5	
		11	$10 + 7 (1 - E/1.5)$	1.25	1.5	
		12	$10 + 13 (1 - E/1.5)$			
		13	$9 + 6 (1 - E/1.5)$			
	2	1-10	hi	$25 - 39.67 E + 58.28 E^2 - 41.18 E^3 + 10.32 E^4$		1.5
			lo	$= \text{hi} / 0.91$		
		11-13	$23 - 32.26 E + 23.16 E^2 - 30.16 E^3 - 11.32 E^4$	1.3	1.4	

Table 1.1: Estimation of errors for φ and ϑ . The errors depend on the number of PEDs per cluster (2. column) and the type of the central crystal of the PED (3. column). In most cases of 2 (or more) PEDs per cluster there is a distinction whether the PED has the largest energy deposit in the cluster (hi) or not (lo). The last column shows the photon energy E_0 up to which the error was parametrized. For higher energies the error at $E = E_0$ is used. The factor F (last but one column) scales the error.

	σ_φ^2	σ_ϑ^2	$\sigma_{\sqrt{E}}^2$
Monte-Carlo	1.57	1.20	1.02
July '92	1.18	1.00	0.97
August '94	1.40	1.10	1.00

Table 1.2: Scaling factors for the errors.

These factors scale the squared errors in order to compensate differences in the data samples and inadequacies of the Monte-Carlo simulation.

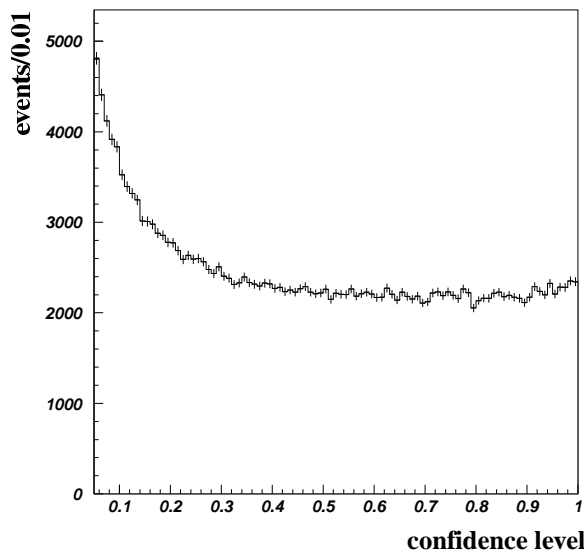


Figure 1.3: Confidence level distribution for the hypothesis $p\bar{p} \rightarrow \pi^0 \pi^0 \pi^0$ at 1940 MeV/c. The distribution should be flat for events which fulfill the hypothesis. The rise at low values originates from events of other reactions, where the fit yields a low confidence level.

1.5. Selection of final states

After the kinematical fit with a free z-vertex events were rejected if none of the final state hypotheses ($3\pi^0$, $2\pi^0\eta$, $\pi^0\eta\eta$, 3η) converged with a confidence level of at least 10% or the fitted z-coordinate of the vertex was outside the target volume ($-5 \text{ cm} < z < 5 \text{ cm}$). The events were classified to originate from a certain kind of reaction according to the hypothesis yielding the highest confidence level. Finally a suppression of 'cross talk' between the final states was applied using the criteria listed in table 1.3.

		confidence level of constraint fit			
		$3\pi^0$	$2\pi^0\eta$	$\pi^0\eta\eta$	3η
classified	$3\pi^0$	>10%	<10 ⁻³	-	-
	$2\pi^0\eta$	<10 ⁻⁵	>10%	-	-
	$\pi^0\eta\eta$	<10 ⁻⁵	<10 ⁻⁵	>10%	<10%
	3η	<10 ⁻⁵	<10 ⁻⁵	<10 ⁻⁵	>10%

Table 1.3: Separation and classification of final states. The table shows upper and lower limits for the confidence level of the tested hypothesis. Emphasized: the restrictive veto cut for the final state $3\pi^0$ against events of the type $2\pi^0\eta$, which accounts for a visible structure in the acceptance in the Dalitz plot (fig.1.4).

With the help of Monte Carlo events undergoing the same chain of reconstruction and selection as real data efficiencies could be estimated. The values for efficiencies and rates for false classification are given in table 1.4. They result as the ratio of the number of classified events of a certain reaction type and the number of generated Monte-Carlo events. The final states $\pi^0\omega$ and $\eta\omega$, where $\omega \rightarrow \pi^0\gamma$,

		generated final state (Monte Carlo)					
		$3\pi^0$	$2\pi^0\eta$	$\pi^0\eta\eta$	3η	$\pi^0\omega$	$\eta\omega$
classified	$3\pi^0$	26.6%	$6 \cdot 10^{-5}$	$2 \cdot 10^{-4}$	$3 \cdot 10^{-5}$	$4 \cdot 10^{-3}$	$3 \cdot 10^{-5}$
	$2\pi^0\eta$	$6 \cdot 10^{-4}$	29.5%	$1 \cdot 10^{-3}$	$6 \cdot 10^{-4}$	$1 \cdot 10^{-3}$	$4 \cdot 10^{-3}$
	$\pi^0\eta\eta$	$3 \cdot 10^{-5}$	$4 \cdot 10^{-5}$	23.5%	$1 \cdot 10^{-3}$	$3 \cdot 10^{-5}$	$6 \cdot 10^{-4}$
	3η	0	$1 \cdot 10^{-5}$	$1 \cdot 10^{-4}$	25.2%	0	$3 \cdot 10^{-5}$

Table 1.4: Efficiencies and 'cross talk'. For each final state with three pseudoscalar mesons approximately 100000 events were simulated and reconstructed, ca. 30000 for each of the background channels with one omega meson.

are considered as the most prominent sources of background[15]. In these cases an electromagnetic split-off is misidentified as a photon. As this background can be suppressed sufficiently no further treatment of split-offs was applied.

Neither in the Dalitz plots nor in the spectra of production angles structures are visible in the acceptance (fig.1.4). The acceptance is almost flat and goes down for production angles close to the beam axis $|\cos\Theta| = 1$. In the final state $\pi^0\pi^0\pi^0$ at $\pi^0\pi^0$ -invariant masses close to the $\pi^0\eta$ -threshold, $m^2 \sim 0.47 \text{ GeV}^2/c^4$, a lack of acceptance is visible in the Dalitz plot. This is due to the restrictive veto cut against events of the type $p\bar{p} \rightarrow \pi^0\pi^0\eta$ (tab. 1.3) which rejects also events of the type $p\bar{p} \rightarrow 3\pi^0$.

1.6. Results of the selection of the 6γ final states at 1.94 GeV/c

The preselection and the selection described above were applied to 10.5 million events taken with an incident antiproton beam momentum of 1.94 GeV/c resulting in 197016 $3\pi^0$ -events, 95285 $2\pi^0\eta$ -events, 5830 $\pi^0\eta\eta$ -events and 472 3η -events (tab. 1.5). The quality of the reconstruction of the

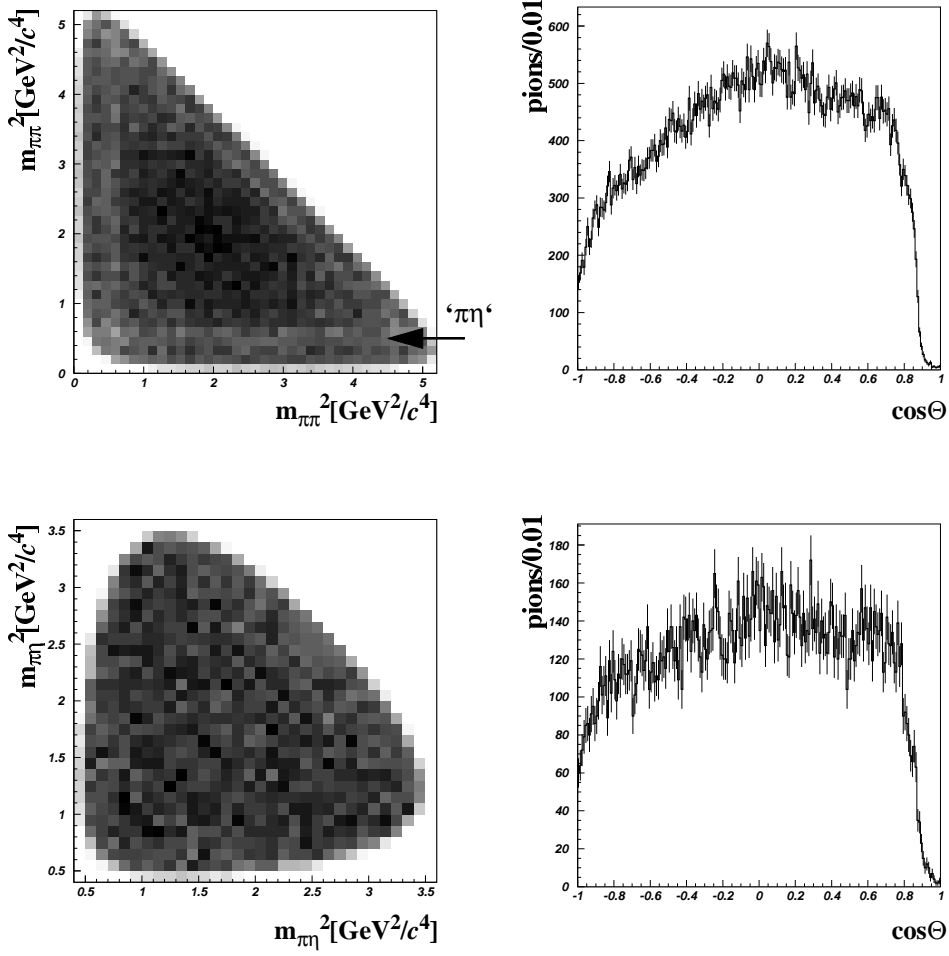


Figure 1.4: Visualization of the acceptance for the final states $3\pi^0$ and $\pi^0\eta\eta$. On the left hand side are shown Dalitz plots for Monte Carlo generated events. In the final state $3\pi^0$ a lack of acceptance originates from a rigorous veto cut against the final state $\pi^0\pi^0\eta$ at $\pi^0\pi^0$ -masses close to the $\pi^0\eta$ -threshold. On the right hand side shown are the distributions of the cosine of the production angle which is defined as the angle between the direction of flight of a pion and the beam axis measured in the overall c.m. system.

data can be demonstrated by the spectrum (fig.1.5) of the two-photon invariant mass in the region of the eta-mass.

1.7. Selection of the final state $3\pi^0$ at $p_{\bar{p}} = 600 \text{ MeV}/c$

For the selection of the data the same procedure was applied as described above. The scaling factors for the errors are listed in table 1.6. The achieved resolution of the 2 photon invariant mass in the region of the η -mass is $13 \text{ MeV}/c^2$. Additional cuts to suppress the background from the reaction $p\bar{p} \rightarrow \pi^0\omega$ were applied:

1. **low-energetic split-offs.** $\pi^0\gamma$ -pairs from the converged fit to the hypothesis $p\bar{p} \rightarrow 2\pi^0 2\gamma$ whose invariant mass lies within the mass window of the ω -meson ($700\text{-}820 \text{ MeV}/c^2$) are selected. If the energy of the photon not belonging to this pair is less than 40 MeV the event is rejected.
2. **Split-offs associated with pions.** If the invariant mass of a $\pi^0\gamma$ -pair of a converged $p\bar{p} \rightarrow 2\pi^0 2\gamma$ hypothesis is smaller than $160 \text{ MeV}/c^2$ the event is rejected.

	July '92		August '94		Σ	
trigger	zero prong	zero prong	mixed(0 or 2 pr.)			
physics events	6327591	3273663	440776			
no charged tracks	5236469	2492941	436816			
6 PEDs	824013	317960	74823			
one hyp. > 0.1	171752	103133	25918			
$\pi^0\pi^0\pi^0$	108211	67773	17099		197016 (193083)	
$\pi^0\pi^0\eta$	52174	32904	8236		95285 (93314)	
$\pi^0\eta\eta$	3220	2032	467		5830 (5719)	
$\eta\eta\eta$	241	171	47		472 (459)	

Table 1.5: Results from the selection at 1940 MeV/c. The table shows the number of events surviving the individual steps of the selection chain for the three different data samples at 1.94 GeV/c. The steps are: recorded physics events, no charged tracks, six PEDs, one final state hypothesis with a confidence level of at least 10%. Below is given the number of events classified as final states. The data sample 'mixed trigger' was already roughly preselected with a veto against charged tracks. As the selection history for a fraction of the data sample from July 1992 is not available due to technical problems the actual number of selected events is slightly larger than the one given in column 2. The right most column shows the total number of really reconstructed events (the sum of the left columns given in brackets).

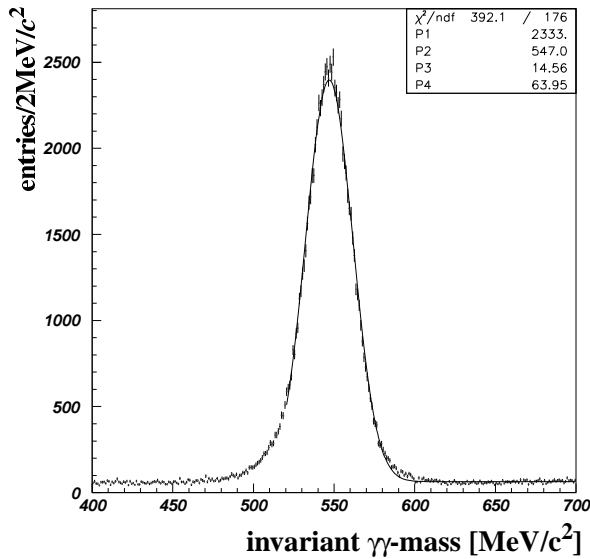


Figure 1.5: Resolution of the $\gamma\gamma$ -invariant mass at 1940 MeV/c. Data taken fulfilled the $2\pi^0\gamma\gamma$ -hypothesis (c.l. > 10%) and have c.l. < 10^{-5} for the $3\pi^0$ -hypothesis. The resolution near the η -mass is $\sigma = 14.6$ MeV/c².

	σ_ϕ^2	σ_θ^2	$\sigma_{\sqrt{e}}^2$
Monte-Carlo	1.40	1.05	0.80
April '93	1.00	1.00	0.80

Table 1.6: Scaling factors for the errors at 600 MeV/c. These factors were determined by the width of pull distributions from the constraint fit as well.

The efficiency for reconstruction and background suppression after these cuts is given in table 1.7. The result of this selection applied to 2964132 events taken in April 1993 is given in table 1.8.

	$\pi^0\pi^0\pi^0$	$\pi^0\omega$ -background
Before background suppression	34.6%	$2.2 \cdot 10^{-3}$
After cut 1	33.1%	$1.8 \cdot 10^{-3}$
After cut 2	32.6%	$8.3 \cdot 10^{-4}$

Table 1.7: Efficiency for reconstruction and background suppression in the $3\pi^0$ -channel at 600 MeV/c. These values are based on a Monte Carlo study using ca. 50000 $\pi^0\pi^0\pi^0$ and 60000 $\pi^0\omega$ events. The table shows clearly that the applied cuts reduce the $\pi^0\omega$ -background by a factor of 3 without any significant impact on the efficiency for reconstruction.

	April '93
trigger	zero prong
physics events	2964132
no charged tracks	2422331
6 PEDs	200334
one hyp. > 0.1	52103
$\pi^0\pi^0\pi^0$	39655
$\pi^0\pi^0\eta$	8637
$\pi^0\eta\eta$	903
$\eta\eta\eta$	4

Table 1.8: Result of the selection at 600 MeV/c. Only the final state $\pi^0\pi^0\pi^0$ was selected.

2. Presentation of the data

2.1. Kinematics of three body reactions in flight

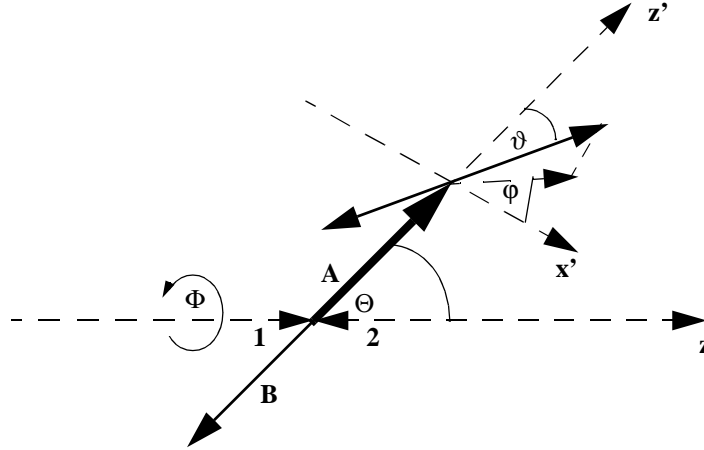


Figure 2.1: Kinematic quantities of three body final states in flight. The positive z -axis is defined by the anti-proton beam direction. In the overall c.m. system a two body system A (bold arrow) is produced with solid angle (Θ, Φ) . In its helicity frame (z' -axis along the direction of flight in the overall c.m. system, x' -axis in the z/z' -plane, two body system is at rest) A decays with spherical angles ϑ and φ .

The phase space for this kind of reaction is four-dimensional. One possible choice of coordinates is the invariant masses squared of two pairs of final state particles (Dalitz plot variables), the polar angle Θ of the direction of flight of a pair measured in the overall c.m. system and the azimuthal angle φ of its decay measured in its helicity frame (fig.2.1). Additionally, within one event, a relative angle Φ can be defined for each of the three different permutations of pairs. Formulas for the calculation of these kinematical quantities are given in appendix A.

2.2. Two-photon invariant masses

The spectrum of the $\gamma\gamma$ invariant mass for events passing a constraint fit to the hypothesis $\bar{p}p \rightarrow 6\gamma$ with a confidence level better than 1% is plotted in figure 2.2. The signals of π^0 and η are clearly visible above the combinatorial background (15 entries per event). The signals from the η' decaying to $\gamma\gamma$ and from the ω decaying $\pi^0\gamma$, where one low-energetic photon from the π^0 decay is not detected, are shown in figure 2.3. In this plot the $\gamma\gamma$ invariant mass is shown from the converged (confidence level > 0.1) hypothesis $\bar{p}p \rightarrow \pi^0\pi^0\gamma\gamma$, where events fulfilling the hypothesis $\bar{p}p \rightarrow \pi^0\pi^0\pi^0$ (confidence level > 0.01) were disregarded. In the mass region 620 to 1000 MeV/ c^2 this spectrum can be described by the sum of two gaussians and a linear term. The gaussian width of the high mass peak (η') gives an estimate for the resolution at high masses: $\sigma = 20.2$ MeV/ c^2 .

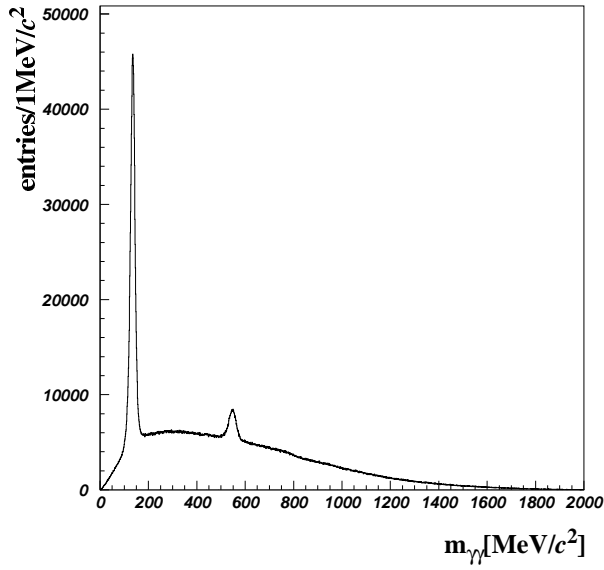


Figure 2.2: $\gamma\gamma$ invariant mass. Above the combinatorial background appear the signals from the π^0 - and the η -meson.

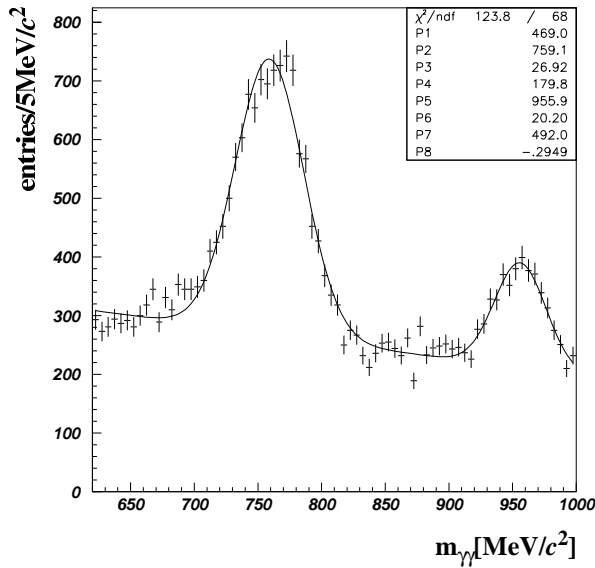


Figure 2.3: Signals from ω and η' seen in the $\gamma\gamma$ invariant mass. The picture shows the region 620 - 1000 MeV/c². A fit of the sum of two gaussians and a linear term yields $\sigma = 20.2$ MeV/c² for the η' peak (958 MeV/c²).

2.3. Spectra of selected final states

2.3.1. $\pi^0\pi^0\pi^0$ at 1940 MeV/c

The Dalitz plot (fig.2.4) has its most prominent structures at the crossings of the interfering $f_2(1270)$ bands. Also the $f_0(975)$ is visible as narrow bands interfering destructively with other structures in the edges of the Dalitz plot. Further structures are a triangularly shaped enhancement at a $\pi^0\pi^0$ invariant mass of 1500 MeV/c² and a diffuse band near the crossing points of the $f_0(975)$ bands close to the edges of Dalitz plot, corresponding to a mass of about 1850 MeV/c². The reduced density of entries at mass squared of ca. 0.47 GeV²/c⁴ is due to the restrictive cut against events of the type $p\bar{p} \rightarrow \pi^0\pi^0\eta$ which rejects events with $\pi^0\pi^0$ invariant masses close to the $\pi^0\eta$ threshold. The spectrum of the invariant $\pi^0\pi^0$ mass (fig.2.5) exhibits the same structures.

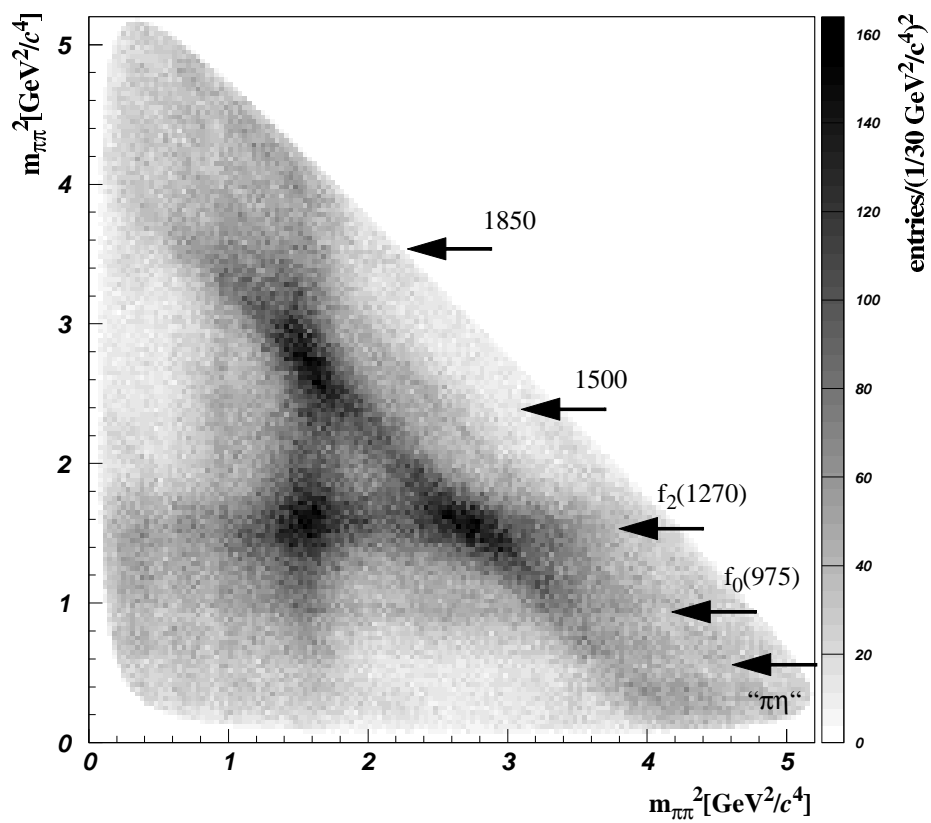


Figure 2.4: Dalitz plot of the reaction $p\bar{p} \rightarrow \pi^0 \pi^0 \pi^0$ at 1940 MeV/c. The signal from the $f_2(1270)$ dominates the plot.

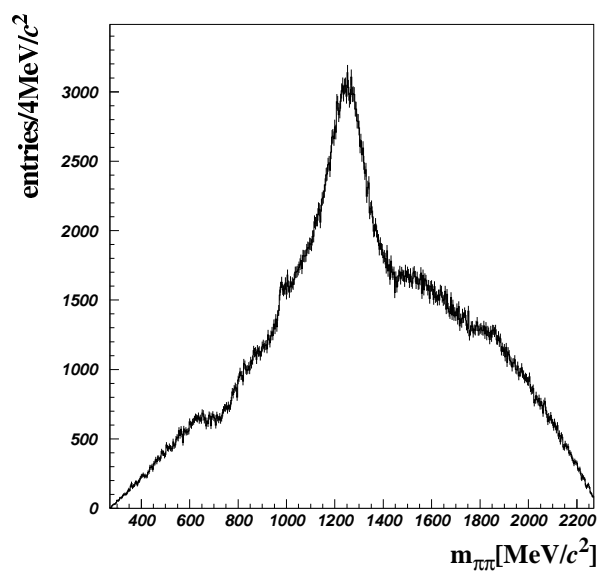


Figure 2.5: Invariant mass $\pi^0 \pi^0$ spectrum in $3\pi^0$ at 1940 MeV/c. The spectrum exhibits the structures also seen in the Dalitz plot.

Figure 2.6 shows the Dalitz plots for different production angles. This representation enhances weak signals in regions where they are not hidden by the angular distributions of stronger signals. So, the

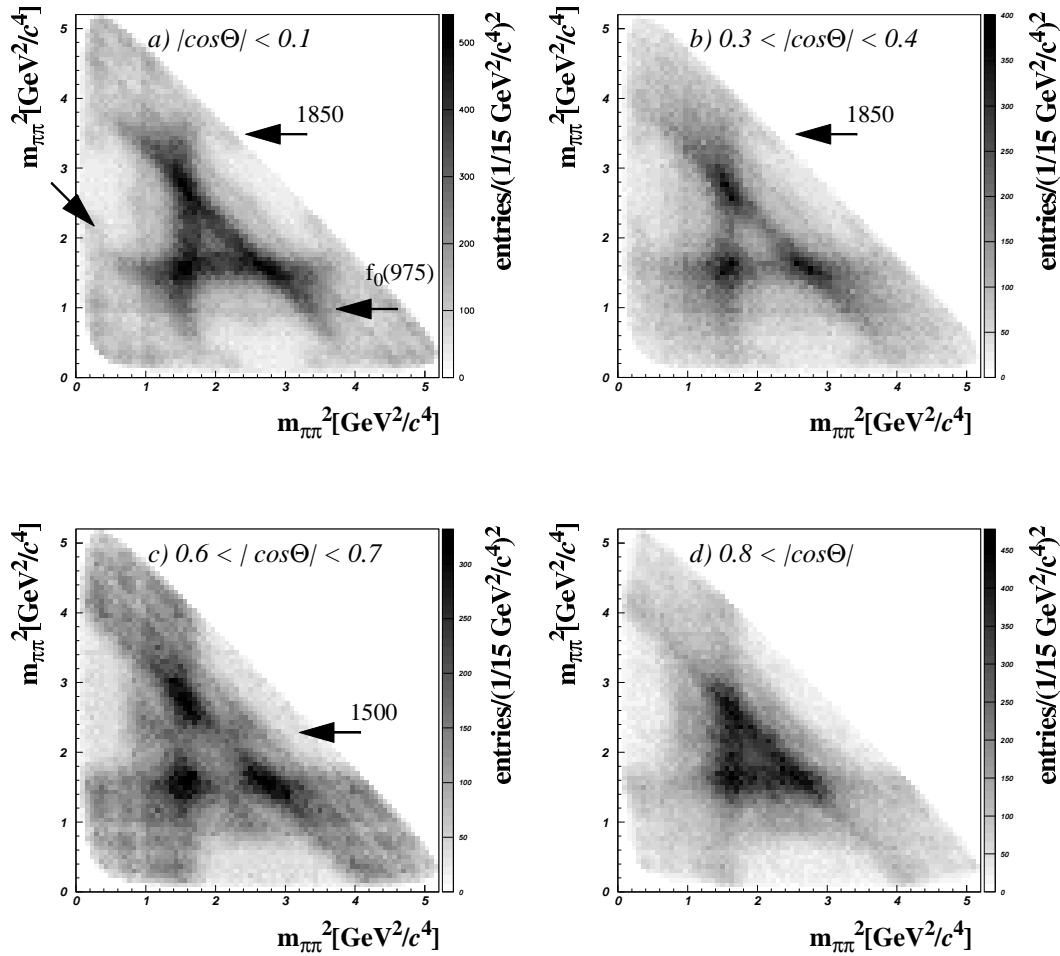


Figure 2.6: Dalitz plot for $p\bar{p} \rightarrow 3\pi^0$ at 1940 MeV/c for different production angles.

cuts on $|\cos\Theta| < 0.1$ and $0.3 < |\cos\Theta| < 0.4$ enhance the structure at 1850 MeV/c² as a band in the Dalitz plot. The signal at 1500 MeV/c² is enhanced in the region $0.6 < |\cos\Theta| < 0.7$.

2.3.2. $\pi^0\pi^0\eta$ at 1940 MeV/c

The Dalitz plot and the spectra of the invariant masses of the reaction $p\bar{p} \rightarrow 2\pi^0\eta$ are shown in figure 2.7. Signals at 1270 MeV/c² and at 1500 MeV/c² in $\pi^0\pi^0$ are visible, also the $a_0(980)$ and the $a_2(1320)$ can be identified by eye. The signal of the $a_0(1450)$ [2] is missing. A very weak structure in the Dalitz plot appears partially hidden by the crossing of the $f_2(1270)$ band with the $a_0(980)$ signal. This corresponds to a $\pi^0\eta$ invariant mass of approximately 1900 MeV/c². This signal can be seen more cleanly in the Dalitz plots of the reactions $p\bar{p} \rightarrow \pi^0\pi^0\eta$ and $p\bar{p} \rightarrow \pi^0\eta\eta$ at $\sqrt{s} = 2980$ MeV/c² measured by the E760 experiment[3] at Fermilab.

2.3.3. $\pi^0\eta\eta$ at 1940 MeV/c

The spectra of the invariant masses and the Dalitz plot of the reaction $p\bar{p} \rightarrow \pi^0 2\eta$ are shown in figure 2.8. Besides the signals from the isovectors $a_0(980)$ and $a_2(1320)$ and a clearly visible band at $\eta\eta$ invariant masses around 1500 MeV/c² there are hints for structures at high $\eta\eta$ masses

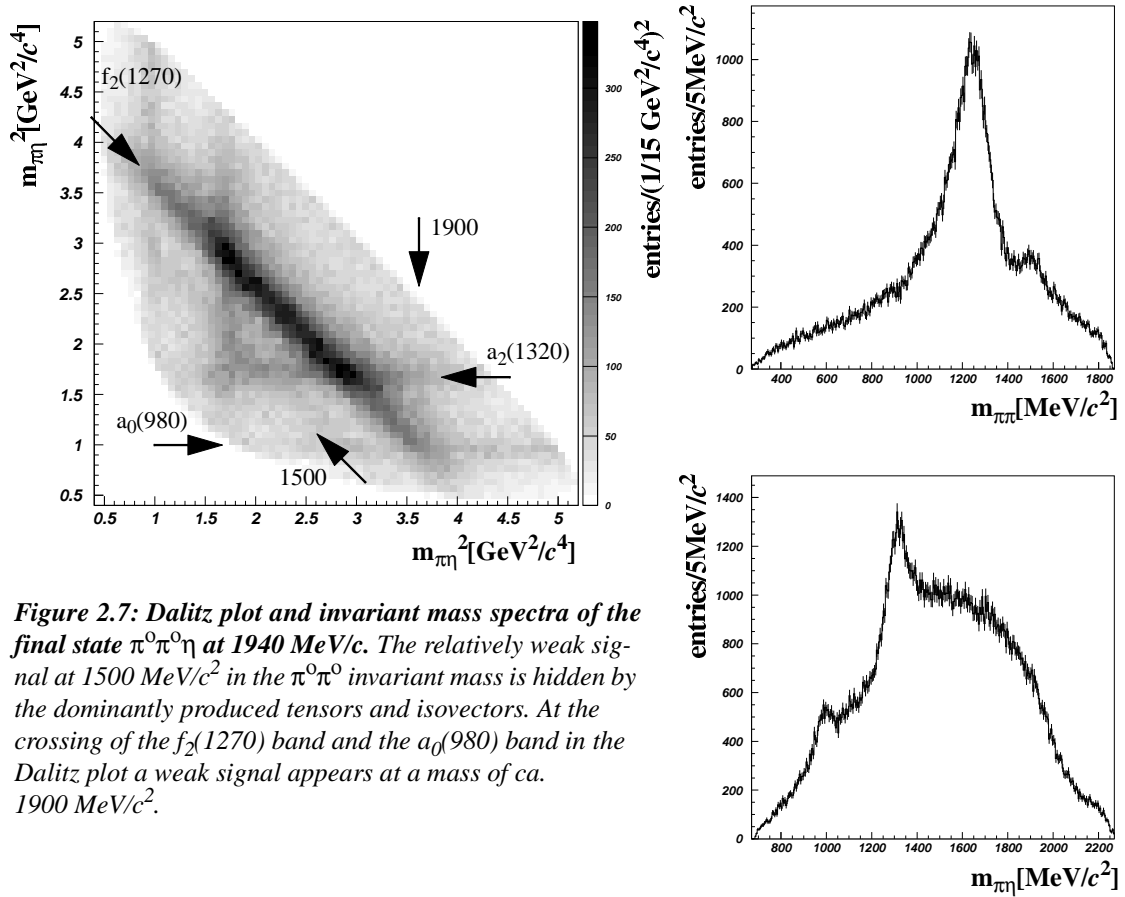


Figure 2.7: Dalitz plot and invariant mass spectra of the final state $\pi^0\pi^0\eta$ at $1940 \text{ MeV}/c$. The relatively weak signal at $1500 \text{ MeV}/c^2$ in the $\pi^0\pi^0$ invariant mass is hidden by the dominantly produced tensors and isovectors. At the crossing of the $f_2(1270)$ band and the $a_0(980)$ band in the Dalitz plot a weak signal appears at a mass of ca. $1900 \text{ MeV}/c^2$.

($2100 \text{ MeV}/c^2$) in the lower left corner of the Dalitz plots strongly hidden by the crossing of the $a_0(980)$ bands. Moreover there is an almost invisible structure at low $\eta\eta$ masses possibly originating from the interfering isovectorial amplitudes. The Dalitz plot is also given in a non-symmetric representation (fig.2.9). The strong enhancement at high $\eta\eta$ masses seems not to be due to the a_0 only.

2.3.4. $\eta\eta\eta$ at $1940 \text{ MeV}/c$

Dalitz plot and the spectrum of the $\eta\eta$ invariant mass are given in figure 2.10. This final state is dominated by a single signal at a mass of $1500 \text{ MeV}/c^2$.

2.3.5. $\pi^0\pi^0\pi^0$ at $600 \text{ MeV}/c$

The Dalitz plot and the spectrum of invariant $\pi^0\pi^0$ mass (fig.2.11) show signals from $f_2(1270)$ and from a state at $1500 \text{ MeV}/c^2$. Like for the Dalitz plot of the reaction $p\bar{p} \rightarrow \pi^0\pi^0\pi^0$ at $1940 \text{ MeV}/c$ there is a lack of acceptance at the $\pi^0\eta$ threshold. Figure 2.12 shows the distribution of the cosine of the production angle for the mass regions $1170 \text{ MeV}/c^2$ to $1370 \text{ MeV}/c^2$ and $1450 \text{ MeV}/c^2$ to $1600 \text{ MeV}/c^2$.

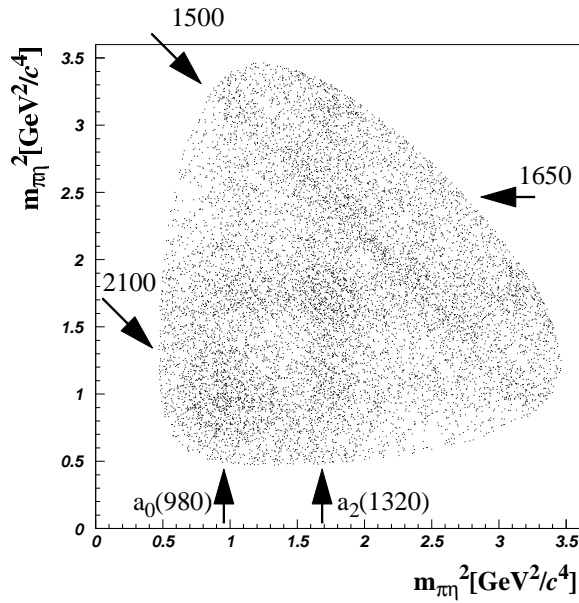


Figure 2.8: Dalitz plot and invariant mass spectra of the final state $\pi^0\eta\eta$ at $1940\text{ MeV}/c$. As the $f_2(1270)$ does not couple strongly to $\eta\eta$ the signal at $1500\text{ MeV}/c^2$ appears clearly in this channel. At the crossing of the a_0 bands in the lower left corner of the Dalitz plot there is an indication for a structure at high $\eta\eta$ masses.

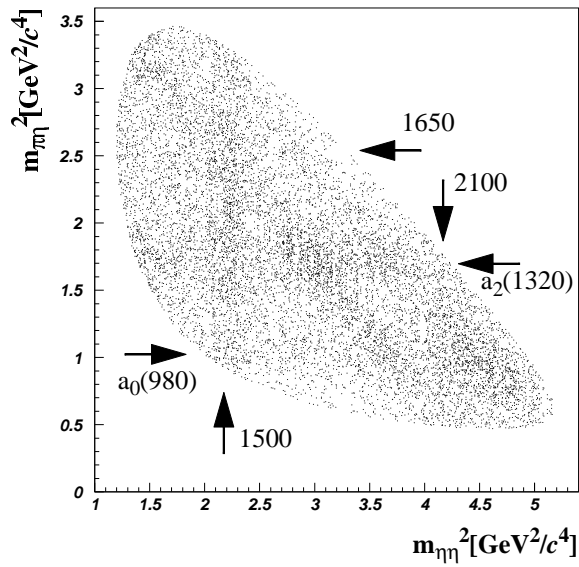
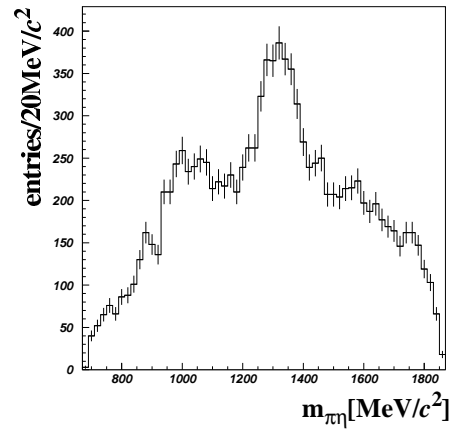
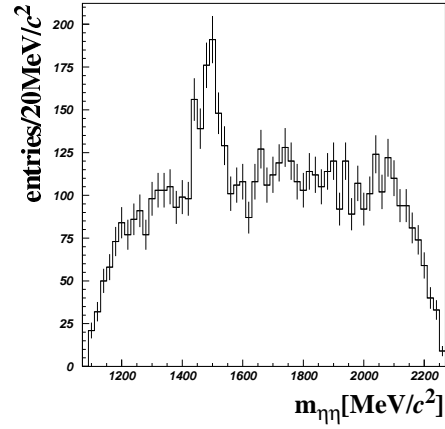


Figure 2.9: Unsymmetrical Dalitz plot of the reaction $p\bar{p}\rightarrow\pi^0\eta\eta$ at $1940\text{ MeV}/c$.

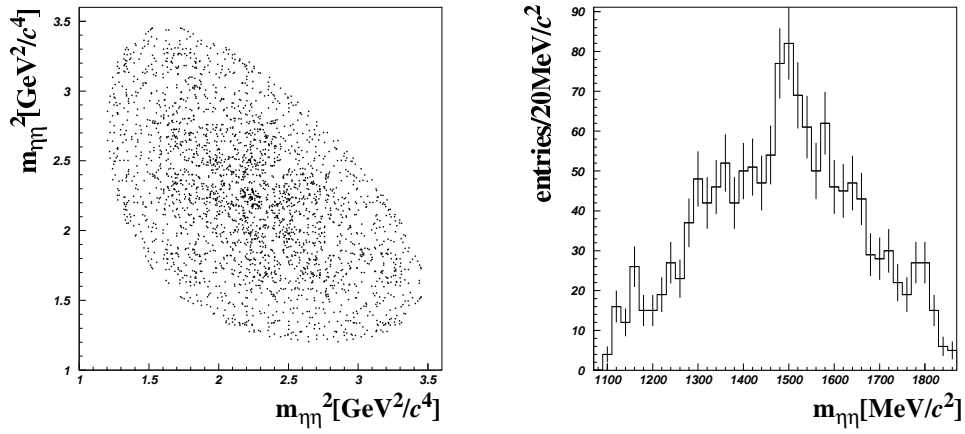


Figure 2.10: The final state $\eta\eta$ at 1940 MeV/c. The signal at 1500 MeV/c² appears as an isolated peak in this channel.

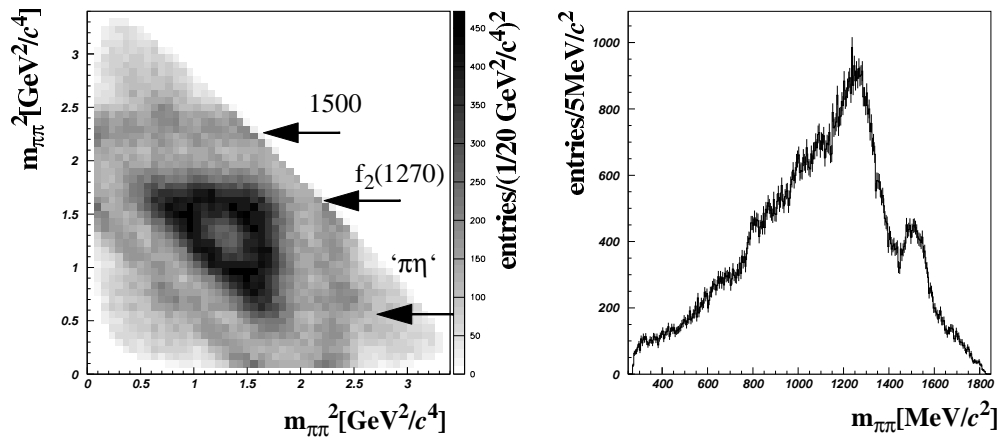


Figure 2.11: Dalitz plot and invariant mass spectrum of the reaction $p\bar{p} \rightarrow \pi^0\pi^0\pi^0$ at 600 MeV/c. The visible structures are the $f_2(1270)$ and a signal at 1500 MeV/c².

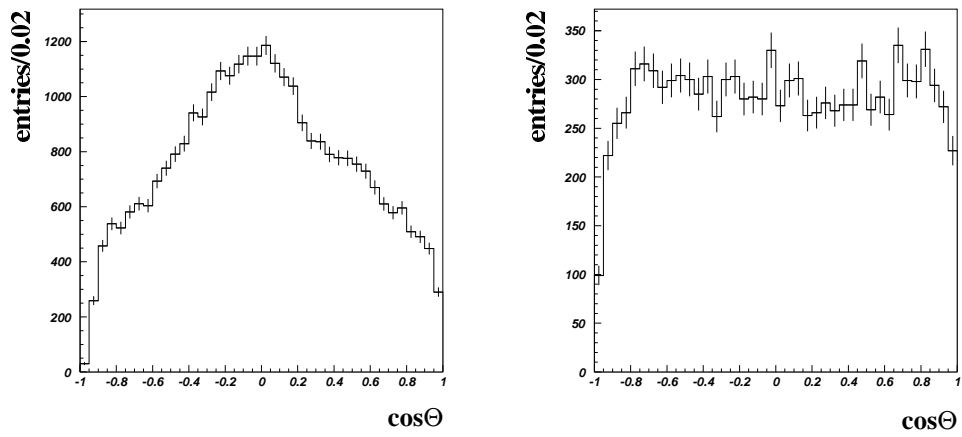


Figure 2.12: Cosine of the production angle for two mass regions. The left figure shows the distribution for masses between $1170 \text{ MeV}/c^2$ and $1370 \text{ MeV}/c^2$, on the right hand side for masses from $1450 \text{ MeV}/c^2$ to $1600 \text{ MeV}/c^2$.

3. Partial wave analysis

The analysis focuses on the reactions $p\bar{p} \rightarrow \pi^0 \eta \eta$ at 1940 MeV/c and $p\bar{p} \rightarrow \pi^0 \pi^0 \pi^0$ at 600 MeV/c. The data at 600 MeV/c can be described using the complete formulation with helicity amplitudes. As many higher spin initial states contribute to $p\bar{p}$ -reactions at 1940 MeV/c a simplified ansatz has to be applied to fit the reaction $p\bar{p} \rightarrow \pi^0 \eta \eta$. This model has already been used to describe the reaction $p\bar{p} \rightarrow \pi^0 \pi^0 \pi^0 \eta$ at 1200 and 1940 MeV/c[14].

The advantage of a complete analysis using helicity amplitudes is that it yields informations about the contributing initial states. Also it tries to describe the distribution of measured events in all four dimensions of phase space.

Symbols and their meaning as they will be used in the following are listed in table 3.1. Some quantities are also explained in figure 2.1. Formulas are given in appendix A.

symbol	meaning
A	intermediate state
B	particle recoiling against A
Θ, Φ	spherical angles of the direction of flight of A as measured in the $p\bar{p}$ c.m. system
ϑ, φ	spherical angles of the direction of flight of one daughter from the decay of A as measured in the rest system of A, where the z-axis is taken to be the direction of flight of A as measured in the $p\bar{p}$ c.m. system (helicity frame)
θ, ϕ	spherical angles of the direction of flight of one daughter from the decay of A as measured in the rest system of A, where the z-axis point parallel to the \bar{p} -beam axis (canonical frame)
m_{ij}, q	invariant mass of particles i and j and the absolute momentum of i in the c.m. system of the reaction $A \rightarrow i+j$
τ	tuple of phase space coordinates of an event
J, P, C	total spin, parity and charge conjugation of the $p\bar{p}$ initial state
L, S, M, v	relative orbital angular momentum between proton and antiproton measured in the $p\bar{p}$ c.m. system, spin of the $p\bar{p}$ systems (0 or 1) with M its projection along the beam axis. v is the helicity of the $p\bar{p}$ system (v = M)
l, l_z	relative orbital angular momentum between A and B as measured in the $p\bar{p}$ c.m. system and its projection along the beam axis
$\sigma, \lambda, \lambda_f$	spin and helicity of A and the projection of spin along the z-axis of the canonical system

Table 3.1: Overview over the used symbols and their meaning. Formulas for the calculation of kinematical quantities are given in the appendix.

The highest contributing angular momenta and the total spin in the $p\bar{p}$ -initial state, respectively, can be estimated in three ways (in units of $\hbar/2\pi$) (tab. 3.2):

	semi-classical L_{\max}	statistical model L_{dom}	measurements J_{\max}
600 MeV/c	1.7	1 - 2	3
1940 MeV/c	5.4	2 - 4	6

Table 3.2: Estimates of the highest contributing spin. The semi-classical ansatz ($b = 1.6$ fm) estimates the maximum orbital angular momentum (L_{\max}), the statistical model ($r = 0.6$ fm) estimates the cross section for annihilation for different partial waves (L_{dom}). From the angular distribution of two-body final states measured in $p\bar{p}$ annihilation in flight[15] an upper limit for the total spin J_{\max} of $p\bar{p}$ system was obtained.

- 1. semi-classical:** assuming an impact parameter b the maximum value of the relative orbital angular momentum L between the proton and the antiproton in the overall c.m. system can be estimated:

$$p \times b = \sqrt{L(L+1)} \frac{h}{2\pi} \quad (3.1)$$

- 2. statistical model:** the statistical model[16] makes predictions about cross sections for individual partial waves (fig.3.1). This model also makes use of eq. 3.1 with an assumed hadronic radius r .

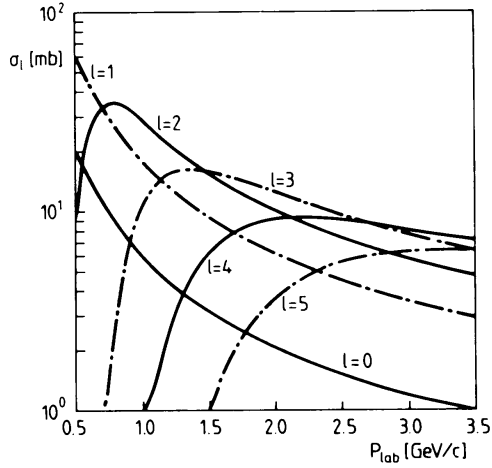


Figure 3.1: Contributing partial waves and their cross section for annihilation. According to this picture F-wave annihilation should dominate the annihilation process at 1.94 GeV/c.

- 3. measurement:** fitting angular distributions in the final states $\omega\pi^0$ and $\omega\eta$ from $p\bar{p}$ annihilation in flight an upper limit for the contributing spin can be given[15].

3.1. Isobar model

An amplitude for a transition of the kind $p\bar{p} \rightarrow m_1 + m_2 + m_3$ is factorized in amplitudes for the subprocesses. Each of these sub-amplitudes again can be factorized as the product of a phenomenological constant being proportional to the Lorentz-invariant matrix element of the transition, a function describing the angular distribution and a dynamical function covering the energy dependence of the amplitude.

$$T_{A \rightarrow BC} = H \cdot F(\Omega) \cdot \Delta(m_{BC}) \quad (3.2)$$

Relativistic Breit-Wigner amplitudes and Blatt-Weisskopf damping factors are used to describe the energy dependence of the amplitudes:

$$\Delta(m_{12}) = B_L(q) \frac{m_0 \Gamma_0}{m_0^2 - m_{12}^2 - i m_0 \Gamma_L(q)} \quad (3.3)$$

$$\Gamma_L(q) = \Gamma_0 \frac{m_0 q}{m_{12} q_0} \frac{B_L^2(q)}{B_L^2(q_0)}, \quad (3.4)$$

with q the momentum of the interacting particles in the c.m. system of the scattering process. The quantities m_0 , Γ_0 and q_0 stand for the nominal values of a resonance: mass, width and decay momentum. The factor $B_L(q)$ are given as[17]:

$$B_0(q) = 1 \quad (3.5)$$

$$B_1(q) = (qr) \left(\frac{2}{1 + (qr)^2} \right)^{1/2} \quad (3.6)$$

$$B_2(q) = (qr)^2 \left(\frac{13}{9 + 3(qr)^2 + (qr)^4} \right)^{1/2}, \dots \quad (3.7)$$

The parameter r is the effective range of the potential in the decay and can be set to $r = 0.2$ fm[18], 0.68 fm[19] or 1 fm[20]. This choice is not crucial as long r is smaller than 1 fm corresponding to a fermi momentum of 200 MeV/ c . In this analysis it is set to be 0.2 fm.

One way to derive the angular dependent term, $F(\Omega)$ in eq. 3.2, is using the helicity formalism[21].

3.1.1. Helicity formalism

Within the helicity formalism the quantization axis is chosen to be the direction of flight of the decaying particle A seen from the c.m. system of the production process of A . The advantage of this choice is that the relative orbital momentum l between the daughter particles has no component along the z -axis. The angular distribution of this decay is then simply given by the D -matrices or D -functions[22]:

$$|m_{12}\lambda_1\lambda_2, \vartheta, \varphi\rangle = D_{M\lambda}^J(\varphi, \vartheta, 0) |m_{12}\lambda_1\lambda_2\rangle \quad (3.8)$$

with J the spin of the mother particle A , M its projection along the z -axis and $\lambda = \lambda_1 - \lambda_2$ the resulting total helicity of the final state. The phenomenological constants H , also called helicity amplitudes are related to constants of the ls -coupling scheme well known from analyses at rest by:

$$H_{\lambda_1\lambda_2}^J = \sum_{l,s} \alpha_{ls}^J \langle s_1\lambda_1 s_2-\lambda_2 | s\lambda \rangle \langle 10s\lambda | J\lambda \rangle \quad (3.9)$$

where s is the total spin of the final state and α_{ls}^J are the ls -coupling coefficients. The sum runs over all contributing orbital angular momenta and spins. The zero in the second Clebsch-Gordan-coefficient is the vanishing projection of l along the z -axis. In the case of the decay into two spinless particles $l = J$, $s = 0$ and therefore $H^J = \alpha^J$ holds. For processes in which the parity is conserved, the following relation holds:

$$H_{-\lambda_1, -\lambda_2}^J = \pi_1 (-1)^{\sigma_1} \pi_2 (-1)^{\sigma_2} P (-1)^J H_{\lambda_1\lambda_2}^J, \quad (3.10)$$

with π_i being the parities of the daughters and σ_i their spins.

For the production of a resonance from the $p\bar{p}$ system in flight and its subsequent decay into two spinless mesons the total amplitude can be written as the product of amplitudes describing the formation of the $p\bar{p}$ scattering state, the transition amplitude of this scattering state into the resonance and a recoiling meson and the decay amplitude of the resonance. For the first subprocess, the formation of the $p\bar{p}$ scattering state, the energy is fixed by the experimental set-up. It can be considered as an reversed decay and is described by the helicity amplitude:

$$\langle a\nu | \nu_1 \nu_2 \rangle = H_{\nu_1\nu_2}^a \quad (3.11)$$

Here ν_1, ν_2 are the helicity substates $\pm 1/2$ of the antiproton and the protons, ν the helicity of the scattering state $\nu = \nu_1 - \nu_2$, and a a short-hand notation for the quantum numbers J, P and C of the system. Following rules are valid for the helicity amplitudes $H_{\nu_1\nu_2}^a$:

- from eq. 3.11 follows: $H_{-\nu_1, -\nu_2}^a = (-1)^{JP} H_{\nu_1\nu_2}^a$, as for the fermion-antifermion-system $\pi_1\pi_2 = -1$ and $\sigma_1 + \sigma_2 = 1$ holds.

- $H_{+ \pm}^a = 0$ for spin singlet states because $S = 0$ and therefore also the spin projections $M = v = 0$ vanish.
- for spin triplet states eq. 3.11 implies $H_{++}^a = -H_{--}^a$. Due to the construction of the wave function for spin triplet states $\psi^a = \frac{1}{\sqrt{2}} (H_{++}^a + H_{--}^a) = 0$ the amplitude for $v = 0$ vanishes.

The amplitude of the resonance production is composed of a helicity amplitude and a D-function. The energy again is fixed as it is the c.m. energy of the $p\bar{p}$ system.

$$\langle c\lambda, \Theta\Phi | a v \rangle = \hat{F}_{\lambda}^b \cdot D_{v\lambda}^{J*}(\Phi, \Theta, 0), \quad (3.12)$$

λ is the helicity of the resonance, the quantum numbers of which are characterized by c , (Θ, Φ) is the solid angle of emission of the resonance and b is a short-hand notation for the tuple of short-hand notations (a, c) . Due to parity conservation the following holds for the helicity amplitudes \hat{F} :

$$\hat{F}_{-\lambda}^b = P(-1)^{J+1} \hat{F}_{\lambda}^b \quad (3.13)$$

For the decay of the resonance a complete amplitude has to be built up containing a helicity amplitude, a D-function and a Breit-Wigner term as well:

$$\langle (\vartheta, \varphi) | c\lambda, m \rangle = f^c \cdot D_{\lambda 0}^{\sigma_c*}(\varphi, \vartheta, 0) \cdot \Delta^c(m), \quad (3.14)$$

with σ_c the spin of the resonance c , m the invariant mass of the pair of daughter particles (ϑ, φ) the solid angle of the decay. Note that the helicity amplitudes f^c exhibits no further indices as the final state particles carry no spin. With $F_{\lambda}^b = \hat{F}_{\lambda}^b \cdot f^c$ the overall amplitude can be written:

$$\begin{aligned} T_{v_1 v_2}(\tau) & \quad (3.15) \\ & = \sum_a H_{v_1 v_2}^a \sum_{k, c} \Delta_c(m_k) \sum_{\lambda} D_{v\lambda}^{J*}(\Phi_k, \Theta_k, 0) D_{\lambda 0}^{\sigma_c*}(\varphi_k, \vartheta_k, 0) \sum_1 \langle 10 \sigma_c \lambda | J \lambda \rangle G_1^b \end{aligned}$$

The helicity amplitudes F_{λ}^b are already expanded in terms of orbital angular momentum l (chap.3.1.1.). With the complex coefficients G_1^b defining the contribution of the corresponding partial waves. The sums extend over all possible permutations k to build select a pair out of three particles. The symbol τ is the tuple of phase space coordinates (2 invariant masses and 2 angles).

Neither \bar{p} nor p are polarized and therefore spin singlet and spin triplet $p\bar{p}$ scattering waves do not interfere. Moreover there are no interferences between transitions with different $p\bar{p}$ magnetic spin substates v . The cross section is hence proportional to:

$$w(\tau) = |T_1(\tau)|^2 + |T_{-1}(\tau)|^2 + 2|T_0^T(\tau)|^2 + 2|T_0^S(\tau)|^2, \quad (3.16)$$

where the lower index of the amplitudes T_v is the $p\bar{p}$ helicity v . An explicit example for a weight function is given in appendix B.1.

3.1.2. Parameters in the helicity formalism

This formalism was used to describe the reaction $p\bar{p} \rightarrow \pi^0 \pi^0 \pi^0$ at an incident antiproton momentum of 600 MeV/c. The parameters involved are:

1. **Helicity amplitudes of the $p\bar{p}$ initial states.** These are complex numbers. Technically they are handled by the program as absolute value and phase.

2. **l-coupling constants** (= **partial wave amplitudes** α). These are also complex numbers. For each resonance having a non-vanishing spin there are for each initial state several possible orbital angular momenta l between the resonance and the recoiling particle.

3. Masses and widths of resonances.

As has been shown previously no higher spins than $J = 2$ are expected to contribute at a beam momentum of 600 MeV/c (tab. 3.2). Therefore only the initial states 1S_0 , 3P_1 , 3P_2 , 1D_2 and 3F_2 were considered to contribute. The state 3P_2 and 3F_2 cannot be distinguished because only the external quantum numbers J , P and C are observable in the final state. The J^{PC} quantum numbers of these states are 0^+ , 1^{++} , 2^{++} and 2^+ . There is only one helicity substate for the 0^+ and 2^+ state each and hence only one helicity amplitude. In the case of the 1^{++} state the amplitude for $v = 0$ vanishes and the other two are not independent (chap.3.1.1.). Only the 2^{++} state has all possible spin substates -1 , 0 and $+1$ which can be parametrized by two independent helicity amplitudes. Note that the production of scalar resonances is forbidden from the 2^{++} state due to parity conservation. The other three states allow scalar resonance production with one partial wave each (tab. 3.3). Tensors can be produced from all four initial states with up to three partial waves from 1D_2 (tab. 3.4).

$\bar{p}p$ -initial state	orbital angular momentum l
$^1S_0(0^+)$	0
$^3P_1(1^{++})$	1
$^3P_2(2^{++})$	-
$^1D_2(2^+)$	2

Table 3.3: Initial states and partial waves for scalar resonances. Scalar resonances cannot be produced from the 3P_2 state.

$\bar{p}p$ -initial state	orbital angular momentum l
$^1S_0(0^+)$	2
$^3P_1(1^{++})$	1,3
$^3P_2(2^{++})$	1,3
$^1D_2(2^+)$	0,2,4

Table 3.4: Initial states and partial waves for tensor resonances. For most of the initial states more than one partial wave is possible.

The number of real parameters is given by

- 10 for the complex helicity amplitudes for the four initial states.
- +6 for the complex partial wave coefficients per scalar resonance.
- +16 for the complex partial wave coefficients per tensor resonance.
- +2 for the mass and the width of each resonance.
- -3 for the freedom of choice of the arbitrary global phases of the three independent incoherently summed terms in eq. 3.16.
- -4 for the normalization of the sums of amplitudes belonging to the individual initial states.

For example a complete fit (free masses and width, all partial waves) with the hypothesis

$$\bar{p}p(0^+, 1^{++}, 2^{++}, 2^+) \rightarrow \pi^0 + [f_2(1270), f_0(1500), f_2(1640)] \quad (3.17)$$

must determine 47 free parameters. This is the reason why typically a first attempt is made to fit the data with a reduced hypothesis, e.g. to fix masses and widths and only allow for contributions of the lowest possible partial waves for each initial state which in this examples would mean 25 free parameters.

The formula obtained from the complete helicity formalism describes the whole process from the production of a resonance from the $\bar{p}p$ scattering state to its decay. It allows to fit the distribution of measured events in all four dimensions of phase space. The limiting feature of this method is the large number of free unknown parameters, especially the partial wave amplitudes, which grows rap-

idly with the number of involved resonances and initial states. A description of the measured reaction $\bar{p}p \rightarrow \pi^0 \eta \eta$ at 1940 MeV/c with this ansatz was not successful. For this reaction a simplified model is used where the angular dependent part of the amplitude is calculated using the canonical formulation.

3.1.3. Canonical description of angular distributions

For a detailed description see CB-note 273[14]. Here we give only a short review. In the canonical formulation the z-axes of all systems are oriented parallel to each other. We discuss again the reaction $\bar{p}p \rightarrow A+B$, where B carries no spin, and the spherical angles of the direction of flight of particle A in the overall c.m. system are (Θ, Φ) (chap.3.1.1.). All four-vectors of the final state particles, measured in the overall c.m. system, are then rotated in such way that the direction of flight of particle A is along the z-axis. This is done by a rotation with Φ around the beam axis and a subsequent rotation with Θ around the new y-axis. After a Lorentz boost anti-parallel to the z-axis (beam axis) which transform all four-vectors into the c.m. system of A the whole system is rotated back by $-\Theta$ and $-\Phi$ (Wick rotation). In this canonical system the spherical angles θ and ϕ of decay are defined as the direction of flight of one daughter of A.

The projection λ_i of the total spin J of the $\bar{p}p$ system must be either -1, 0 or 1 because the relative orbital angular momentum is perpendicular to the beam axis. As the $\bar{p}p$ -initial state is not polarized there is no interference between these three spin substates. With l being the orbital angular momentum between A and B in the overall c.m. system and l_z its projection along the z-axis (beam axis), as well as λ_f the projection of spin s of particle A along the z-axis, the angular dependent part of the transition amplitude from a $\bar{p}p$ -initial state can be expressed using Clebsch-Gordan coefficients:

$$|J, \lambda_i\rangle = \sum_{\lambda_f, l_z, l} \langle s \lambda_f | l_z | J \lambda_i \rangle |s, \lambda_f\rangle |l, l_z\rangle \quad (3.18)$$

The eigenstate of angular momentum is represented by a Legendre polynomial

$$|l, l_z\rangle = P_l^{l_z}(\Theta, \Phi) , \quad (3.19)$$

and the state of the decay products

$$|s, \lambda_f\rangle = P_s^{\lambda_f}(\theta, \phi) , \quad (3.20)$$

with (θ, ϕ) the solid angle of the decay in the c.m. system of particle A. Due to conservation of the total magnetic spin sub-quantum number M in the process amplitudes to different λ_i add up incoherently.

The coherent summation of amplitudes belonging to the same λ_f is correct assuming all transitions coming from interfering initial states without relative phases. As this ansatz will be applied to a considerably large set of $\bar{p}p$ -initial states the sum should take into account that there are also incoherent parts contributing to the cross section as well as coherent ones with different phases. The simplification in this ansatz is now to fit the amount of interference between two amplitudes of the same λ_f as a free parameter. In the case of two interfering amplitudes e.g. instead just to fit the strengths a and b of the two amplitudes and their relative phase an additional parameter c_{ab} is introduced which describes the amount of interference:

$$I = a^2|A|^2 + b^2|B|^2 + c_{ab} ab (\cos \varphi_{ab} \Re(AB^*) + \sin \varphi_{ab} \Im(AB^*)) , \quad (3.21)$$

where the value of c_{ab} is limited to the interval -2 to +2. An explicit example of a weight function is given in appendix B.2.

3.1.4. Parameters in the canonical approach

The canonical formulation with the mentioned simplification was applied to fit the reaction $\bar{p}p \rightarrow \pi^0 \eta \eta$ at 1940 MeV/c. This approach is attractive due to the reduced number of free variables in

the fit. For each resonance with spin σ there are $\sigma+1$ real parameters. Additional parameters are introduced to take interferences into account. They describe the relative phases between interfering amplitudes and the strength of interference. By this method interferences can be switched on and off whenever it is clear that interferences must be included or can be omitted (e.g. if the bands of the resonances do not overlap in the Dalitz plot). In example (3.17) there would be six free parameters with no interferences. Masses and widths are fixed due to the software implementation. They have to varied ‘by hand’. Giving freedom to the fit to adjust all interferences there are 5 additional real parameters for the interfering strengths and 3 further parameters for relative phases. The number of parameters (in this example 20 including masses and widths) is independent of the assumed initial states in the hypotheses and does only depend on the number of resonances involved.

3.2. Likelihood fit

The fit of the amplitudes to the data was performed using *maximum likelihood* methods. If p is the probability to observe an event at an elementary phase space volume at point τ , then the probability P to observe a set of events distributed according to a weight function $p = w(\tau, \mathbf{x})$ (\mathbf{x} the vector of adjustable parameters) is given by the product of all probabilities multiplied by $n!$ (n = number of events) as the order of events does not matter. The likelihood is defined in the same sense for weight function representing probability densities with arbitrary normalization:

$$L = n! \prod_{i=1}^n \frac{w(\tau_i, \hat{\mathbf{x}}) \varepsilon(\tau_i)}{\int w(\tau, \hat{\mathbf{x}}) \varepsilon(\tau) d\tau} \quad (3.22)$$

Acceptance of the apparatus and efficiency of reconstruction are described by ε , the free parameters in the weight function by $\hat{\mathbf{x}}$. The integral in the denominator extends over the kinematically allowed region of the multi dimensional phase space. The product runs over all measured events i at phase space point τ_i . The integral is needed to normalize the weight function and prevent it from diverging during the fitting procedure. For technical reasons the quantity to be minimized is taken to be the *negative logarithmic likelihood* NLL

$$\text{NLL}' = -\log L. \quad (3.23)$$

The integral $\Theta = \int w(\tau, \hat{\mathbf{x}}) \varepsilon(\tau) d\tau$ is approximated numerically via the summation of the weight function over a sample of Monte Carlo events. As these undergo the same influences of acceptance and efficiency as the data the factor ε is already considered implicitly. With m the number of Monte Carlo events the approximation reads

$$\Theta \cong \frac{n}{m} \sum_{j=1}^m w(\tau_j^{\text{MC}}, \hat{\mathbf{x}}) = \frac{n}{m} \Phi. \quad (3.24)$$

By neglecting all constant terms (terms not depending on \mathbf{x}) which do not affect the optimization procedure the calculated value of NLL is:

$$\text{NLL}' = - \sum_{i=1}^n \log(w(\tau_i, \hat{\mathbf{x}})) + n \log\left(\frac{\Phi}{m}\right). \quad (3.25)$$

In order to allow for the statistical error in the number of measured events and to normalize the phase space integral the so called generalized likelihood function[23]:

$$L_G = e^{-\frac{(n-\Theta)^2}{2n}} L \quad (3.26)$$

is used. After purging all non-interesting terms from the formula the expression to be finally minimized reads:

$$\text{NLL} = \frac{n}{2} \left(\frac{\Phi}{m} - 1 \right)^2 - \sum_{i=1}^n \log(w(\tau_i, \hat{x})) + n \log \left(\frac{\Phi}{m} \right). \quad (3.27)$$

In case of convergence of the minimization procedure $\Phi = m$ holds and the first and third term vanish.

An improvement in NLL of 0.5 by extending the hypotheses by r more free variables corresponds to a change of one in the reduced χ^2 to r degrees of freedom. Therefore a reduction of NLL of more than 0.5 per added fit parameter has to be considered as significant (one standard deviation). Similarly the error of a fitted parameter can be estimated by scanning it in the neighborhood of the found value (all other parameters fixed). Ideally the NLL should behave like a parabola. In a distance of one (two) standard deviation σ the value of NLL increases by 0.5 (2).

For fitting the minimization package MINUIT[24] was used. For the complete helicity fits the MIGRAD method was chosen, for the canonical approach FUMILI.

4. Results of the analysis

4.1. The reaction $p\bar{p} \rightarrow \pi^0\pi^0\pi^0$ at 600 MeV/c

Analysis in terms of helicity amplitudes

The steps in the analysis procedure are summarized in table 4.2 on page 31. The different fits to different hypotheses can be compared by the value of NLL only. The χ^2 value considers only the two dimensions of the Dalitz plot. Therefore the effort to calculate χ^2 correctly was not undertaken. The sixfold symmetry of the Dalitz plot as well as the multiple counting of events contributing to cells along the symmetry axes of the Dalitz plot were not taken into account. As already mentioned the contributing intermediate states which are visible in figure 2.11 are the $f_2(1270)$ and a state with mass = 1500 MeV/c². The flat angular distribution of the latter as it is observed in the Dalitz plot indicates its spin to be zero. The simplest hypothesis one can think of is to describe this reaction with an intermediate $f_2(1270)$ and the $f_0(1500)$ known from our analyses at rest. Simple semi-classical arguments and predictions from calculations done within the framework of a statistical model hint to an upper limit of 2 for the spin in the initial state. Therefore only $J^{PC} = 0^+, 1^{++}, 2^{++}$ and 2^+ are taken into consideration. This first attempt restricts to the lowest partial waves (angular momentum l between f_2 and recoil pion) for each initial state and uses fixed masses and widths of the resonances.

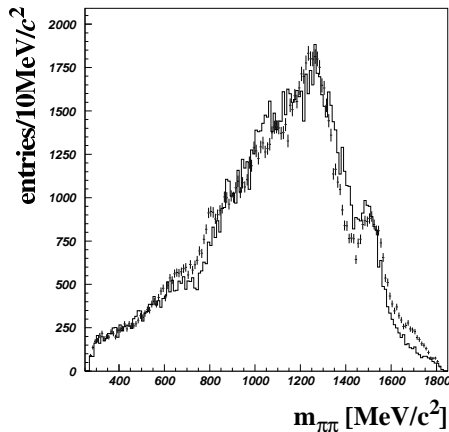


Figure 4.1: $\pi^0\pi^0$ invariant mass spectrum. The plot shows the result of the simplest fit. Real data are shown as error bars, the solid line indicates the fit result.

Fig. 4.1 shows the result of the fit for the $\pi^0\pi^0$ -invariant mass spectrum. It becomes evident that the measured data cannot be described by this hypothesis. The reduced χ^2 of the Dalitz plot fit is 6.8, the value of $NLL = -7520.8$. Masses and widths of both resonances were fixed to 1270 MeV/c² and 185 MeV/c² for the $f_2(1270)$ and 1500 MeV/c² and 100 MeV/c² for the $f_0(1500)$, respectively.

The next step was to allow all partial waves, i.e. higher orbital angular momenta between the $f_2(1270)$ and the recoiling pion. This results in $NLL = -8516.7$ and a reduced χ^2 of 4.9. Starting from this result and varying masses and widths of the resonances yields improved values $NLL = -9001.7$ and a reduced χ^2 of 3.5 (fig.4.2).

Not only due to the NLL and χ^2 value this result is not acceptable. The width of the $f_0(1500)$ is determined to be 242 MeV/c² and thus too broad. This is typical for a situation where the hypothesis is too simple and the fitter tries to cover other structures with a broad Breit-Wigner shape.

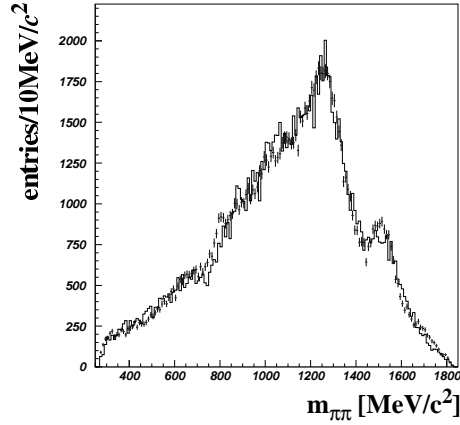


Figure 4.2: $\pi^0\pi^0$ -invariant mass spectrum. The fit shows the result of the simplest hypothesis with all partial waves and free masses and widths.

A significant improvement can be achieved by adding amplitudes for a further tensor resonance. Starting with a $f_2(1270)$ with a mass of $1270 \text{ MeV}/c^2$ and a width of $185 \text{ MeV}/c^2$, a $f_0(1500)$, $M = 1500 \text{ MeV}/c^2$, $\Gamma = 100 \text{ MeV}/c^2$ and a tensor resonance f_2' , $M = 1540 \text{ MeV}/c^2$, $\Gamma = 150 \text{ MeV}/c^2$ with fixed masses and widths $\text{NLL} = -9280$ can be reached. Allowing for the variation of the three masses improves the result to $\text{NLL} = -9475.1$, where the masses turn out to be 1257 , 1533 and $1620 \text{ MeV}/c^2$ respectively. Finally varying additionally resonance widths results in $\text{NLL} = -9510.8$ and a reduced χ^2 of 1.64 with 44 parameters all together.

Masses, widths and the contribution of resonances and initial states as given by this fit are listed in table 4.1. Here all resonance contributions from one initial state are summed coherently, separately

		$f_2(1270)$	$f_0(1500)$	f_2'	initial state contribution
mass		$1260 \pm 2 \text{ MeV}/c^2$	$1534 \pm 2 \text{ MeV}/c^2$	$1640 \pm 4 \text{ MeV}/c^2$	
width		$179 \pm 4 \text{ MeV}/c^2$	$131 \pm 4 \text{ MeV}/c^2$	$169 \pm 8 \text{ MeV}/c^2$	
1S_0		4.2%	19.0%	1.1%	26.1%
3P_1	$1 = 1$	0.2%	6.6%	0.1%	7.4%
	$1 = 3$	0.5%		0.2%	
3P_2	$1 = 1$	25.2%		10.4%	36.1% (0.39)
	$1 = 3$	1.3%		1.1%	
1D_2	$1 = 0$	27.1%		0.8%	30.4%
	$1 = 2$	1.9%	0.1%	0.1%	
	$1 = 4$	0.2%		< 0.1%	
fraction		60.8%	24.6%	14.6%	

Table 4.1: Fit result for the reaction $p\bar{p} \rightarrow \pi^0\pi^0\pi^0$ at $600 \text{ MeV}/c$. The table shows the fractions of the contributing partial waves. Errors of masses and widths determined by the fit are also given. The value in brackets in the right most column gives the relative fraction from the initial state 3P_2 originating from helicity substate $v = 0$.

for the initial state's helicity substates v in order to determine the relative contribution of the initial states. The summation was always carried out by summing over $3\pi^0$ Monte Carlo events distributed according phase space without detector simulation. To determine the contribution of each resonance all amplitudes belonging to it were summed according to the rules of the helicity formalism, coher-

ently and incoherently. The contribution of single partial waves were calculated without taking into account any interferences and normalizing them to the incoherent sum.

Dalitz plot, spectrum of the invariant mass and distribution of production angle for different mass regions are shown in figure 4.3. It is obvious that this hypothesis is able to reproduce simultaneously

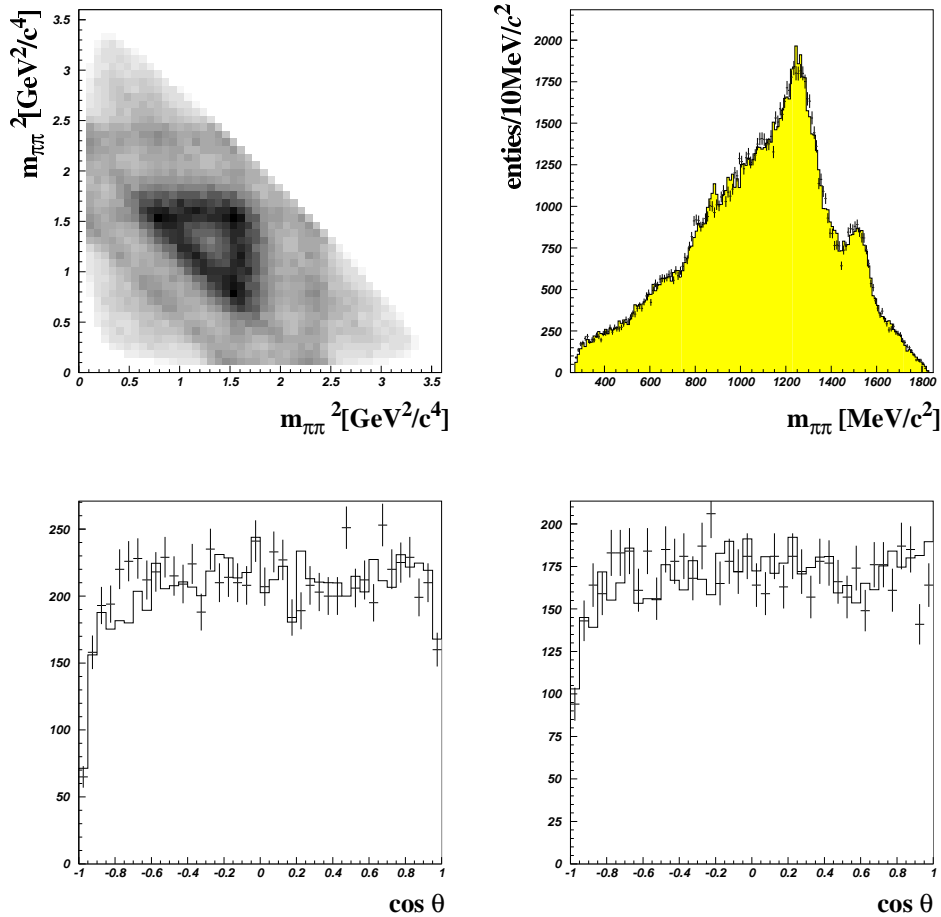


Figure 4.3: Spectra from the best fit. The upper left plot shows the fitted Dalitz plot, the upper right plot the fitted spectrum of the $\pi^0\pi^0$ invariant mass. The measured data are indicated by error bars, the solid line shows the fit result. The lower row shows the distributions of the cosine of the production angle for $\pi^0\pi^0$ invariant mass regions $1450 \text{ MeV}/c^2 - 1550 \text{ MeV}/c^2$ and $1550 \text{ MeV}/c^2 - 1750 \text{ MeV}/c^2$.

the measured event density at high and at low masses. It also explains the production and decay angular distributions of the dominant structures.

An attempt to describe the data with a new scalar resonance replacing the new tensor results in $NLL = -9240.1$ and a reduced χ^2 of 2.7 for the Dalitz plot description. The result is shown in figure 4.4. Mass and width of the additional scalar are determined to be $1685 \text{ MeV}/c^2$ and $277 \text{ MeV}/c^2$ respectively with great uncertainties. The width of the $f_0(1500)$ reaches here the value $88 \text{ MeV}/c^2$, which is not in agreement with other measurements, e.g. the $3\pi^0$ -data from $p\bar{p}$ annihilation at rest.

In figures 4.5 the χ^2 distribution in the Dalitz plot is shown for the best fit. Both plots do not show any structure.

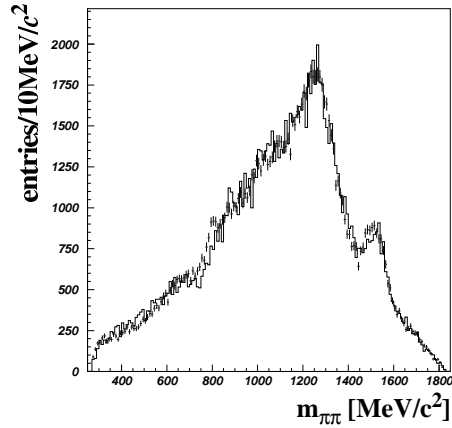


Figure 4.4: Result from the spin-zero hypothesis for the third intermediate state. With this hypothesis the mass distribution can be described in the high mass region of the spectrum only.

	parameter	hypothesis	NLL	red. χ^2
f_2, f_0	14	$^1S_0, ^3P_1, ^3P_2, ^1D_2$ $f_2(1270), f_0(1500)$ only lowest partial wave	-7520.8	6.8 (fig.4.1)
	22	all partial waves	-8516.7	4.9
	26	masses and widths	-9001.7	3.5 (fig.4.2)
f_2, f_0, f_0'	28	$^1S_0, ^3P_1, ^3P_2, ^1D_2$ $f_2(1270), f_0(1500), f_0'$ all partial waves	-9024.2	
	31	masses	-9216.0	
	34	widths	-9240.1	2.7 (fig.4.4)
f_2, f_0, f_2'	38	$^1S_0, ^3P_1, ^3P_2, ^1D_2$ $f_2(1270), f_0(1500), f_2'$ all partial waves	-9280.0	
	41	masses	-9475.1	
	44	widths	-9510.8	1.64 (fig.4.3)

Table 4.2: Fit results of different hypotheses. The data require the assumption of an additional 2^{++} resonance. A scalar particle instead can not reproduce the measured event density.

In figure 4.6 the contributions of the individual initial states to the Dalitz plot are shown. The contributions of the three resonances are shown in figure 4.7.

4.2. The reaction $p\bar{p} \rightarrow \pi^0 \eta \eta$ at 1940 MeV/c

Analysis in terms of the canonical description

The spectra of the data are shown in chap. 2.3.3. on page 15. Due to the high spins in the initial states the complete helicity formalism could not be applied successfully to fit these data. The simplified ansatz using the canonical formulation was used instead. With this method only the intermediate state can be studied but not the initial states nor the partial wave contribution. Here again the starting point was the simplest reasonable hypothesis in order to describe the most dominant features of the measured Dalitz plot. These are the signals of the $a_0(980)$, the $a_2(1320)$ and the $f_0(1500)$. The progress of this analysis is shown in table 4.3.

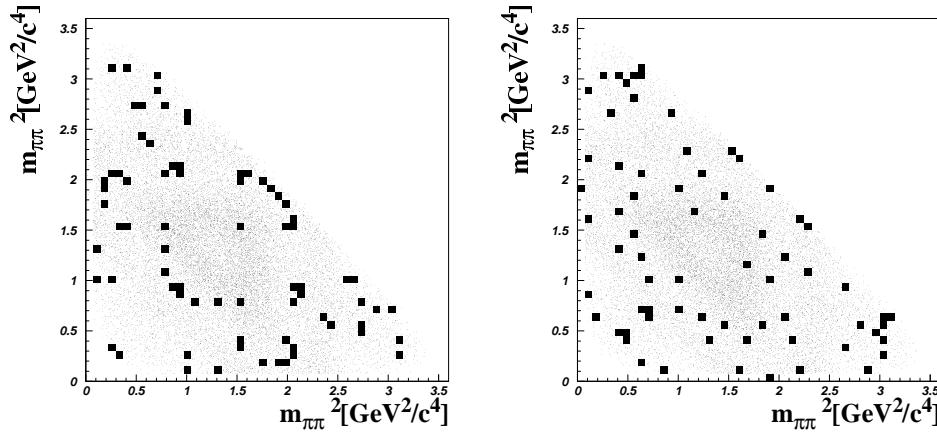


Figure 4.5: χ^2 -distribution in the Dalitz plot. Cells with a χ^2 larger than 4 corresponding three standard deviations are marked black. The left picture shows the cells with more intensity in the fit result than in measured data, the right one the cells where there more intensity is exhibited by the real data than by theory. The background shows the measured Dalitz plot.

The first attempt fits the three parameters of the $a_2(1320)$ amplitudes and the three parameters for the amount of coherence of these amplitudes with themselves. Self-coherence means the interference between the amplitude evaluated for one $\pi^0\eta$ -combination with the same amplitude taken for the other $\pi^0\eta$ -pair. One parameter is added for the $f_0(1500)$ intensity and another one for the $a_0(980)$ signal. Later on, interferences between all three resonances are included and the relative phases. The strength of self-coherence of the $a_0(980)$ is fixed to a value of 1.5. Masses and widths of the isovectorial resonances are set to the values listed in [1]: $M = 984 \text{ MeV}/c^2$ and $\Gamma = 85 \text{ MeV}/c^2$ for the a_0 and $M = 1318.2 \text{ MeV}/c^2$, $\Gamma = 113 \text{ MeV}/c^2$ for the a_2 . The f_0 is fixed to values $M = 1490 \text{ MeV}/c^2$ and $\Gamma = 100 \text{ MeV}/c^2$ which is a rough estimate from the $\eta\eta$ invariant mass spectrum. Fitting this amplitude yields a NLL value of 277. The result of this fit is shown in figure 4.8. The χ^2 for the comparison of measured and the fitted Dalitz plot is 2242.3 for 723 cells and 11 free parameters. It can be seen clearly that this fit does not describe the data. The differences are drastic at high $\eta\eta$ masses and at $\pi^0\eta$ masses at $1600 \text{ MeV}/c^2$. This is reflected in the low $\eta\eta$ mass region.

Note that only the NLL value is used for the comparison of fit results. The method of χ^2 test is not appropriate due the lack of statistics. Moreover the NLL uses the unbinned position of individual events in the Dalitz plot, the χ^2 does not. The value of the χ^2 is again calculated ignoring the fact of multiple entries per event in cells along the diagonal and double counting of events due to the symmetry of the Dalitz plot histogram. It is just an approximate estimate for the quality of a fit as the absolute scale of the NLL value is arbitrary.

Adding an isoscalar tensor with $M = 2100 \text{ MeV}/c^2$ and $\Gamma = 200 \text{ MeV}/c^2$ and with a relative phase and interference with the $a_0(980)$ improves the NLL significantly to -25.3. The χ^2 of this fit is 1771 for 723 cells and 16 free parameters. Varying the self-coherence strengths of the $a_0(980)$ results in a NLL of -32.2 at maximum coherence of the $a_0(980)$ amplitudes. The optimization of this hypothesis ends up with allowing the fit to adjust the relative phase of the $f_0(1500)$ amplitude and yields NLL = -79.9 and $\chi^2 = 1739.2$ for 723 cells and 18 free parameters. The spectra from this fit are shown in figure 4.9.

There is too much intensity at high $\eta\eta$ masses generated by the newly introduced tensor resonance, but the $a_0(980)$ signal is reproduced fairly well. The remaining differences between data and theory at low $\eta\eta$ invariant masses and high $\pi^0\eta$ invariant masses indicate the possible existence of a new isovector with about $M = 1600 \text{ MeV}/c^2 - 1700 \text{ MeV}/c^2$. This became subject of a fit using an extended hypothesis which assumes an additional $a_2(1650)$ with $M = 1650 \text{ MeV}/c^2$ and $\Gamma = 240 \text{ MeV}/c^2$.

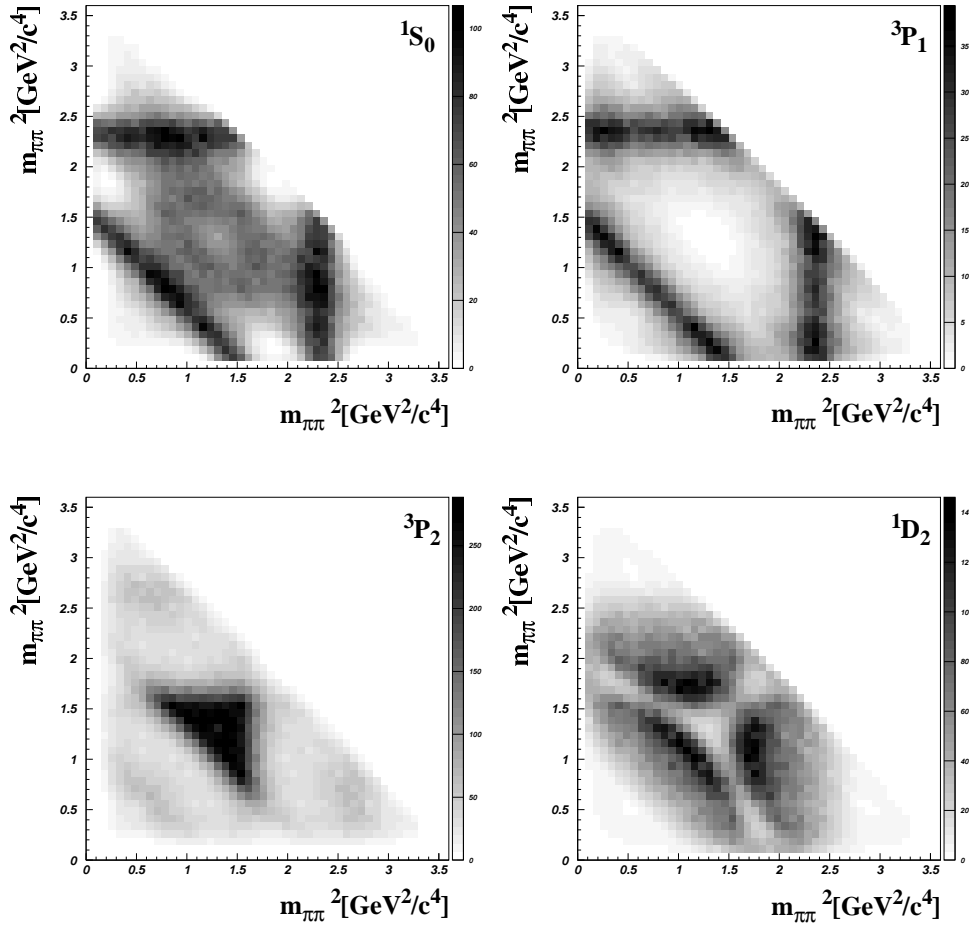


Figure 4.6: Contributions of the initial states to the Dalitz plot according to the best fit. The 3P_1 initial state contributes most to the $f_0(1500)$ whereas the 1D_2 initial state produces dominantly the $f_2(1270)$. The signals of the new $f_2(1640)$ show up in the corners of the Dalitz plot of the 3P_2 contribution.

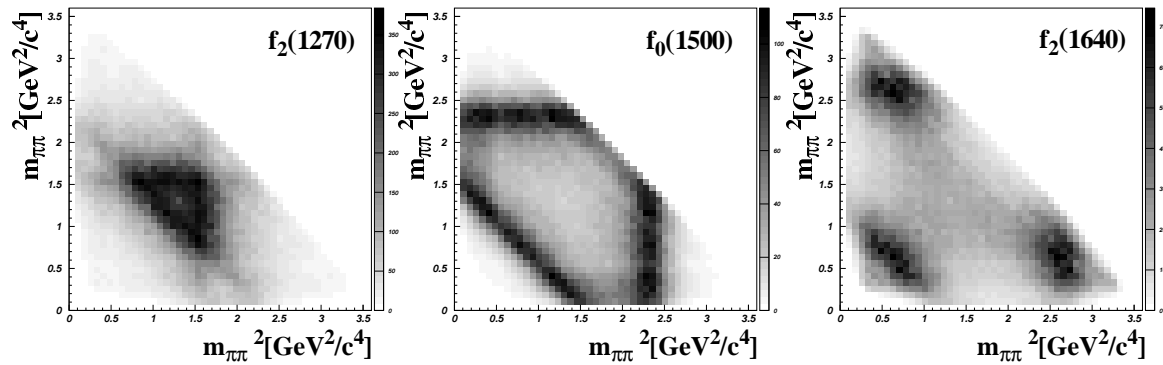


Figure 4.7: Dalitz plot intensities of the resonances contributing to the best fit. MonteCarlo simulated events are filled into the histograms weighted with the fitted intensity from the amplitudes of single resonances.

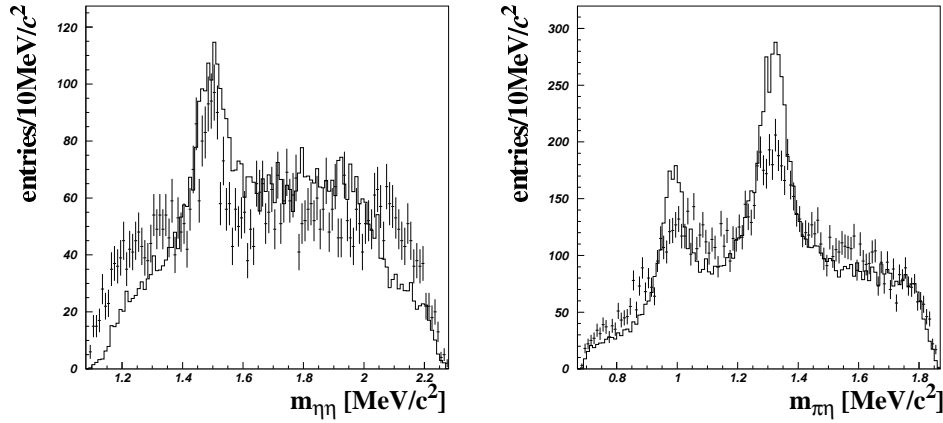


Figure 4.8: *Invariant mass spectra of the final state $\pi^0\eta\eta$. The error bars shows the distribution of real data. The fit result is given as solid line. Obviously there are more than three intermediate states involved in the reaction.*

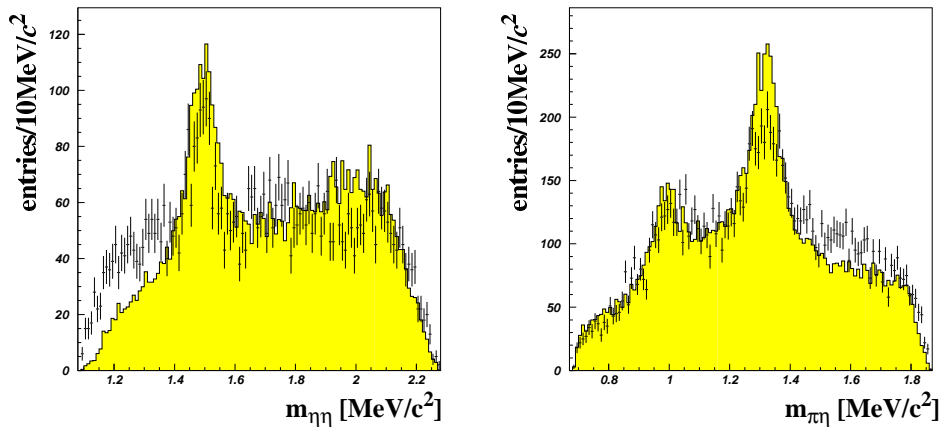


Figure 4.9: *Mass spectra from a fit with a heavy tensor state. The signal of the $a_0(980)$ can now be described well by the interference of the crossing band of the heavy tensor. But there is too much calculated intensity at high $\eta\eta$ masses. Still the fit cannot explain the mass distribution at $1600 \text{ MeV}/c^2$ in the $\pi^0\eta$ invariant mass.*

This fit describes the data much better using additional eight free parameters for the $a_2(1650)$ intensity, its interference with the $a_2(1320)$ and the $f_0(1500)$ and its relative phase. The resulting NLL is -446.6 with $\chi^2 = 1376$ at 723 cells and 26 free parameters. The mass spectra (fig.4.10) are now reproduced much better. The weak point of this fit is the description of the event density at the edges of the phase space at low $\eta\eta$ masses and high $\pi^0\eta$ masses.

Further improvement is achieved by adding intensity from the $f_0(975)$ with $M = 975 \text{ MeV}/c^2$ and $\Gamma = 60 \text{ MeV}/c^2$, the phase of its amplitude and the strength of interference with the $a_2(1320)$ and the $a_2(1650)$. The NLL drops to -528.9 at a χ^2 of 1200 at 723 cells and 30 free parameters. A Breit-Wigner amplitude for a resonance far below the $\eta\eta$ threshold is tried in order to achieve a parametrization of threshold effects due to unitarity conservation. By adjusting masses and widths of the $f_0(1500)$, the $f_2(2100)$ and the $a_2(1650)$ to $(1477, 142)$, $(2135, 245)$ and $(1650, 260) \text{ MeV}/c^2$, respectively, a good fit is obtained (fig.4.11). The lowest value of NLL reaches -553.4 with $\chi^2 = 1153.8$ at finally 36 adjusted parameters.

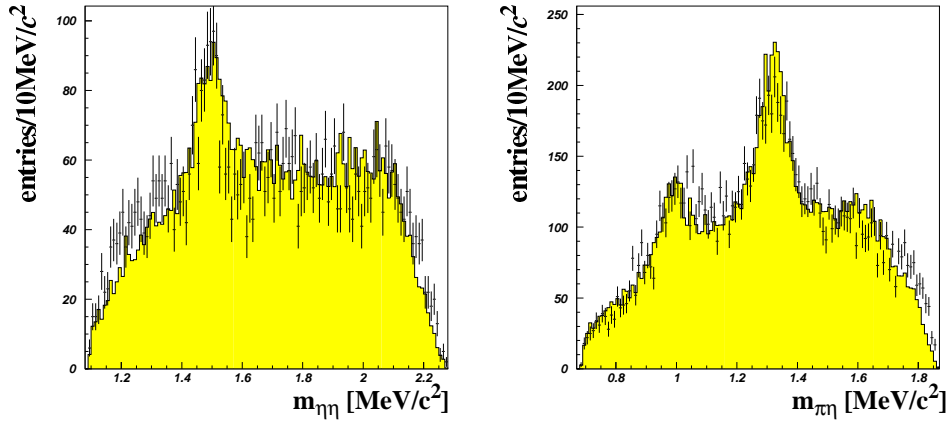


Figure 4.10: Mass spectra with a new isovector. A significant improvement can be achieved by adding a new tensorial isovector state.

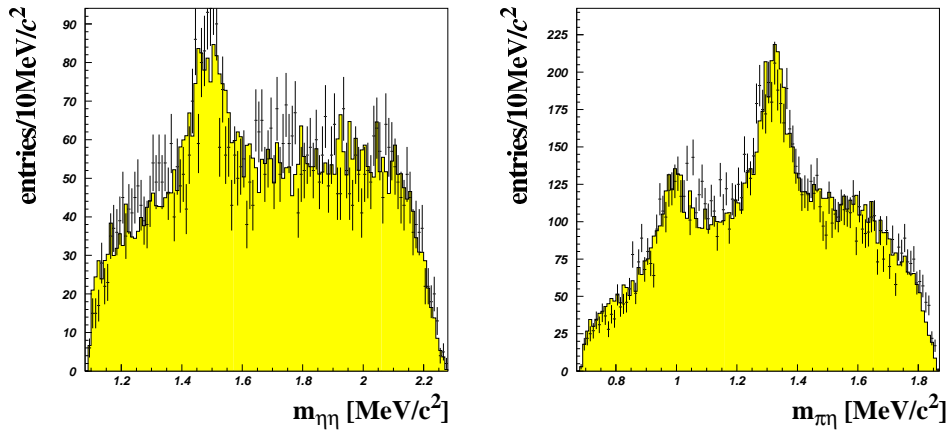


Figure 4.11: Mass spectra from the final fit result.

Masses and widths of the final fit are listed in table 4.4. The estimated errors of the masses and widths are extracted from the study of the behaviour of the NLL values in the neighborhood of the optimum. In figure 4.12 the dependence of the NLL values of masses and widths of the $f_0(1500)$, the new isovector and the heavy isoscalar is shown. As the NLL behaves as a real parabola only near the minimum the error can only be estimated in very approximate manner.

In table 4.5 the results of best fits assuming different spins for the intermediate states $f(2100)$ and $a(1650)$ are listed. Spin 2 is preferred for the description of $a(1650)$, but for $f(2100)$ the results for spin 2 and spin 4 are equivalent. Any further distinction is not possible with the data available. Also the spin 0 fit for $f(2100)$ yielding a much worse value of NLL should not be completely excluded. It turns out that the few amount of events in the corner of phase space with strong interferences cannot be used to draw any conclusion about the spin of this resonance. I personally favor the spin 2 solution because the additional parameters for the spin 4 fit lead to no significant improvement.

parameter	hypothesis	NLL	χ^2
11	$a_0(980), a_2(1320), f_0'(1500)$ interferences $a_0+a_2, f_0'+a_2, a_2+a_2$ Phase a_2	277.0	2242.3 (fig.4.8)
16	$f_2'(2100)$ interferences a_0+f_2' phase f_2'	-25.3	1795.4
17	interference a_0+a_0	-32.2	1771.3
18	phase f_0'	-79.9	1739.2 (fig.4.9)
26	$a_2'(1650)$ interference $f_0'+a_2', a_2+a_2'$ phase a_2'	-446.6	1376.0 (fig.4.10)
30	$f_0(975)$ interference f_0+a_2, f_0+a_2' phase f_0	-528.9	1200.0
36	masses and widths	-553.4	1153.8 (fig.4.11)

Table 4.3: Proceeding of the analysis $\bar{p}p \rightarrow \pi^0 \eta \eta$ at 1940 MeV/c. The assumption of further resonances improves the quality of the description significantly.

	mass	width
$f_0(1500)$	$1477 \pm 6 \text{ MeV}/c^2$	$142 \pm 8 \text{ MeV}/c^2$
$f_2(2100)$	$2135 \pm 5 \text{ MeV}/c^2$	$245 \pm 10 \text{ MeV}/c^2$
$a_2(1650)$	$1650 \pm 15 \text{ MeV}/c^2$	$260 \pm 15 \text{ MeV}/c^2$

Table 4.4: Masses and widths from the best fit. The errors can be estimated very roughly only.

spin hypothesis	NLL
f_2, a_0	-490.1
f_0, a_2	-488.1
f_2, a_2	-553.4
f_4, a_2	-554.6

Table 4.5: Comparison of different spin assumptions for $f(2100)$ and $a(1650)$. Spin 4 requires two further parameters to describe the heavy isoscalar. A clear distinction between spin 2 and 4 is therefore not possible.

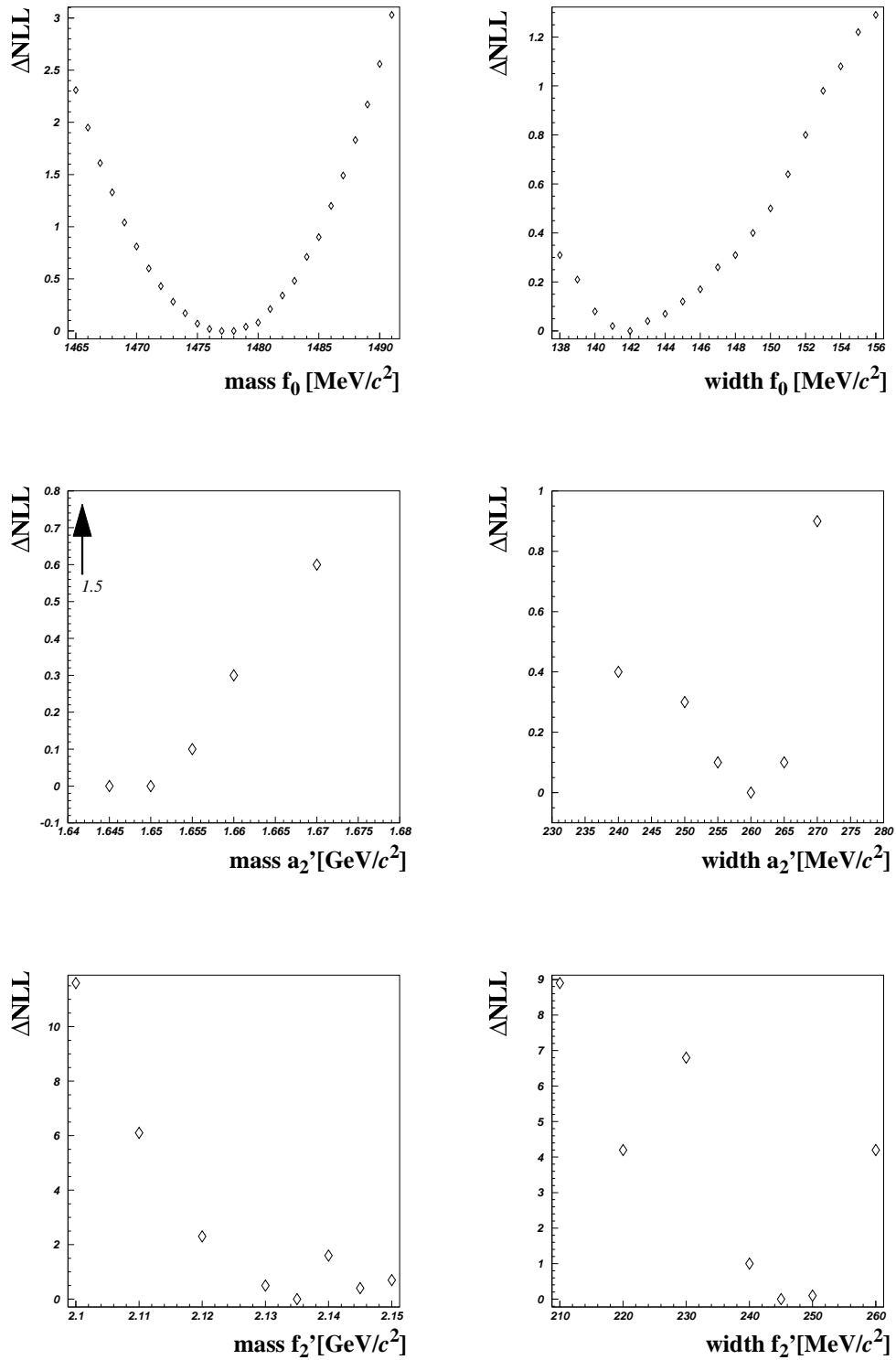


Figure 4.12: Dependence of the value of ΔNLL of mass and widths. Ideally the NLL behaves as a parabola near the optimum.

A Formulae for kinematic quantities

The experiment measures the four-vector components of the three pseudoscalar mesons $p_i = (e_i, \vec{p}_i)$. The invariant mass of a meson pair is given by:

$$m_{ij}^2 = (p_i + p_j)^2 = e_i e_j - \vec{p}_i \vec{p}_j, \quad \vec{p}_i = (x_i, y_i, z_i). \quad (4.1)$$

As all quantities are measured in the laboratory frame they boosted to the overall c.m. system of the reaction by applying a Lorentz transformation:

$$p_i' = L_z(-p_z) p_i = \begin{bmatrix} \gamma & 0 & 0 & -\beta\gamma \\ 0 & 1 & 0 & 0 \\ 0 & 0 & 1 & 0 \\ -\beta\gamma & 0 & 0 & \gamma \end{bmatrix} \begin{bmatrix} e_i \\ x_i \\ y_i \\ z_i \end{bmatrix} \quad (4.2)$$

with β the velocity of the $p\bar{p}$ system in the laboratory frame in units of the speed of light c and $\gamma = \frac{1}{\sqrt{1-\beta^2}}$ the corresponding relativistic dilatation factor. Given a system with rest mass m , absolute momentum p and energy e in any frame the relativistic quantities in the same frame are then $\beta = p/e$ and $\gamma = e/m$ and hence $\beta\gamma = p/m$. For $p\bar{p}$ annihilation in flight at 1940 MeV/ c their values are:

$$\beta = 0.627, \quad \gamma = 1.284, \quad \beta\gamma = 0.805. \quad (4.3)$$

The four-vector of a meson pair in the overall c.m. system is the sum of the two vector of the mesons:

$$r_{ij}' = p_i' + p_j'. \quad (4.4)$$

The spherical angles Θ and Φ of production of this pair are given by:

$$\cos\Theta_{ij} = \frac{z_i' + z_j'}{|\vec{r}_{ij}'|}, \text{ and} \quad (4.5)$$

$$\sin\Phi_{ij} = \frac{y_i' + y_j'}{\sqrt{(x_i' + x_j')^2 + (y_i' + y_j')^2}}$$

$$\cos\Phi_{ij} = \frac{x_i' + x_j'}{\sqrt{(x_i' + x_j')^2 + (y_i' + y_j')^2}}.$$

In order to obtain the four-vector p_i' and p_j' of the decay production in their common c.m. system they are rotated by $-\Phi$ around the beam axis and then by $-\Theta$ around the y -axis of the overall c.m. system. Afterwards all vector are boosted by $L_z(-r_{ij}'')$:

$$\vec{p}_i'' = \mathbf{R}(0, -\Theta, -\Phi) \vec{p}_i' = \begin{bmatrix} \cos\Theta \cos\Phi & \cos\Theta \sin\Phi & -\sin\Theta \\ -\sin\Phi & \cos\Phi & 0 \\ \sin\Theta \cos\Phi & \sin\Theta \sin\Phi & \cos\Theta \end{bmatrix} \begin{bmatrix} x_i' \\ y_i' \\ z_i' \end{bmatrix} \quad (4.6)$$

$$p_i''' = L_z(-r_{ij}''') p_i'' \quad (4.7)$$

The spherical angles ϑ and φ of the resonance decay in the helicity frame are given analogously to eq. 4.5:

$$\cos\vartheta_{ij} = \frac{z_i'''}{\left| \vec{p}_i''' \right|}, \text{ etc.} \quad (4.8)$$

In the canonical formulation a subsequent rotation has to be applied:

$$\tilde{p}_i = \mathbf{R}(0, \Theta, \Phi) p_i''' \quad (4.9)$$

B Formulae used in the best fits

B.1. Weight function for the reaction $p\bar{p} \rightarrow \pi^0 \pi^0 \pi^0$ at 600 MeV/c

$$\begin{aligned}
 w(\tau) = & \left[\begin{aligned} & \frac{1}{\sqrt{2}} (H_{++}^{0^*} - H_{--}^{0^*}) \left(\sum_{k=1}^3 \Delta_{f_0}(m_k) G_0^{0^*, f_0} \right. \\ & \left. + \sum_{k=1}^3 \Delta_{f_2}(m_k) G_2^{0^*, f_2} + \sum_{k=1}^3 \Delta_{f_2'}(m_k) G_2^{0^*, f_2'} \right) \\ & + \frac{1}{\sqrt{2}} (H_{++}^{2^*} - H_{--}^{2^*}) \left(\sum_{k=1}^3 \Delta_{f_0}(m_k) D_{00}^2(\Omega_k) G_2^{2^*, f_0} \right. \\ & \left. + \sum_{k=1}^3 \Delta_{f_2}(m_k) \sum_{\lambda=-2}^2 D_{0\lambda}^2(\Omega_k) D_{\lambda 0}^2(\omega_k) \sum_{l=0,2,4} \langle 102\lambda|2\lambda \rangle G_1^{2^*, f_2} \right. \\ & \left. + \sum_{k=1}^3 \Delta_{f_2'}(m_k) \sum_{\lambda=-2}^2 D_{0\lambda}^2(\Omega_k) D_{\lambda 0}^2(\omega_k) \sum_{l=0,2,4} \langle 102\lambda|2\lambda \rangle G_1^{2^*, f_2'} \right) \end{aligned} \right] \quad 2 \\
 & + \left[\begin{aligned} & \frac{1}{\sqrt{2}} (H_{++}^{2^*} + H_{--}^{2^*}) \\ & \left(\sum_{k=1}^3 \Delta_{f_2}(m_k) \sum_{\lambda=-2}^2 D_{0\lambda}^2(\Omega_k) D_{\lambda 0}^2(\omega_k) \sum_{l=1,3} \langle 102\lambda|2\lambda \rangle G_1^{2^*, f_2} \right. \\ & \left. + \sum_{k=1}^3 \Delta_{f_2'}(m_k) \sum_{\lambda=-2}^2 D_{0\lambda}^2(\Omega_k) D_{\lambda 0}^2(\omega_k) \sum_{l=1,3} \langle 102\lambda|2\lambda \rangle G_1^{2^*, f_2'} \right) \end{aligned} \right] \quad 2 \\
 & + \left[\begin{aligned} & H_{+-}^{1^*} \left(\sum_{k=1}^3 \Delta_{f_0}(m_k) D_{-10}^1(\Omega_k) G_1^{1^*, f_0} \right. \\ & \left. + \sum_{k=1}^3 \Delta_{f_2}(m_k) \sum_{\lambda=-1}^1 D_{-1\lambda}^1(\Omega_k) D_{\lambda 0}^2(\omega_k) \sum_{l=1,3} \langle 102\lambda|1\lambda \rangle G_1^{1^*, f_2} \right. \\ & \left. + \sum_{k=1}^3 \Delta_{f_2'}(m_k) \sum_{\lambda=-1}^1 D_{-1\lambda}^1(\Omega_k) D_{\lambda 0}^2(\omega_k) \sum_{l=1,3} \langle 102\lambda|1\lambda \rangle G_1^{1^*, f_2'} \right) \\ & \left. + H_{-+}^{2^*} \left(\sum_{k=1}^3 \Delta_{f_2}(m_k) \sum_{\lambda=-2}^2 D_{-1\lambda}^2(\Omega_k) D_{\lambda 0}^2(\omega_k) \sum_{l=1,3} \langle 102\lambda|2\lambda \rangle G_1^{2^*, f_2} \right) \right] \quad 2 \\
 & + \left[\begin{aligned} & H_{+-}^{1^*} \left(\sum_{k=1}^3 \Delta_{f_0}(m_k) D_{10}^1(\Omega_k) G_1^{1^*, f_0} \right. \\ & \left. + \sum_{k=1}^3 \Delta_{f_2}(m_k) \sum_{\lambda=-1}^1 D_{-1\lambda}^1(\Omega_k) D_{\lambda 0}^2(\omega_k) \sum_{l=1,3} \langle 102\lambda|1\lambda \rangle G_1^{1^*, f_2} \right. \\ & \left. + \sum_{k=1}^3 \Delta_{f_2'}(m_k) \sum_{\lambda=-1}^1 D_{1\lambda}^1(\Omega_k) D_{\lambda 0}^2(\omega_k) \sum_{l=1,3} \langle 102\lambda|1\lambda \rangle G_1^{1^*, f_2'} \right) \\ & \left. + H_{-+}^{2^*} \left(\sum_{k=1}^3 \Delta_{f_2}(m_k) \sum_{\lambda=-2}^2 D_{-1\lambda}^2(\Omega_k) D_{\lambda 0}^2(\omega_k) \sum_{l=1,3} \langle 102\lambda|2\lambda \rangle G_1^{2^*, f_2} \right) \right] \quad 2
 \end{aligned}$$

This weight function is used in the best fit (see chap. 4.1., table 4.1 and figure 4.3). The symbols are defined in chap. 3.1.1., Ω_k substitutes $(\Phi_k, \Theta_k, 0)$, ω_k substitutes $(\phi_k, \vartheta_k, 0)$. Free parameters of the fit are all partial wave amplitudes G_l , the helicity amplitudes H of the initial states and the nominal values of resonance masses and widths, which are implicitly contained in the dynamical functions Δ .

The hypothesis of the fit assumes contributions of the initial states $J^{PC} = 0^+, 1^{++}, 2^{++}$ and 2^+ and of the resonances $f_0(1500)$, $f_2(1270)$ and $f_2'(1640)$. The first expression in the sum in the formula given above is the contribution from the spin singlet $\bar{p}p$ -scattering states, the second considers contributions from spin triplet amplitudes with helicity substate $v = 0$ (here only transitions from 3P_2 to π^0 -tensor appear). The last two expressions contain the amplitudes from transitions from spin triplet initial states with helicity substates $v = -1$ and $v = +1$.

B.2. Weight function for the reaction $\bar{p}p \rightarrow \pi^0 \eta \eta$ at 1940 MeV/c

$$\begin{aligned}
w(\tau) = & a_{f_0}^2 |\Delta_{f_0}(m_{\eta\eta})|^2 + a_{f_0'}^2 |\Delta_{f_0'}(m_{\eta\eta})|^2 + \sum_{\lambda_f=0,1,2} a_{f_2, \lambda_f}^2 |\Delta_{f_2, \lambda_f}(m_{\eta\eta}) P_2^{\lambda_f}(\theta_{\eta\eta}, \phi_{\eta\eta})|^2 \\
& + a_{a_0}^2 \left(|\Delta_{a_0}(m_1)|^2 + |\Delta_{a_0}(m_2)|^2 + c_{a_0 a_0} e^{i\varphi_{a_0 a_0}} \Delta_{a_0}(m_1) \Delta_{a_0}^*(m_2) \right) \\
& + \sum_{\lambda_f=0,1,2} a_{a_2, \lambda_f}^2 \left| \sum_{k=1,2} \Delta_{a_2, \lambda_f}(m_k) P_2^{\lambda_f}(\theta_k, \phi_k) \right|^2 + \\
& \sum_{\lambda_f=0,1,2} a_{a_2, \lambda_f}^2 \left(|\Delta_{a_2, \lambda_f}(m_k) P_2^{\lambda_f}(\theta_1, \phi_1)|^2 + |\Delta_{a_2, \lambda_f}(m_k) P_2^{\lambda_f}(\theta_2, \phi_2)|^2 \right) + \\
& \sum_{\lambda_f=0,1,2} a_{a_2, \lambda_f} c_{a_2 a_2, \lambda_f} e^{i\varphi_{a_2 a_2, \lambda_f}} \Delta_{a_2, \lambda_f}(m_1) \Delta_{a_2, \lambda_f}^*(m_2) P_2^{\lambda_f}(\theta_1, \phi_1) P_2^{\lambda_f*}(\theta_2, \phi_2) \\
& + \sum_{k, k'=1,2} a_{a_0} a_{a_2, 0} c_{a_0 a_2} e^{i\varphi_{a_0 a_2}} \Delta_{a_0}(m_k) \Delta_{a_2}^*(m_{k'}) P_2^0(\theta_{k'}, \phi_{k'}) \\
& + \sum_{k=1,2} a_{a_0} a_{f_2'} c_{a_0 f_2'} e^{i\varphi_{a_0 f_2'}} \Delta_{a_0}(m_k) \Delta_{f_2'}^*(m_{\eta\eta}) P_2^0(\theta_{\eta\eta}, \phi_{\eta\eta}) \\
& + \sum_{k=1,2} a_{f_0} a_{a_2, 0} c_{f_0 a_2} e^{i\varphi_{f_0 a_2}} \Delta_{f_0}(m_{\eta\eta}) \Delta_{a_2}^*(m_k) P_2^0(\theta_k, \phi_k) \\
& + \sum_{k=1,2} a_{f_0'} a_{a_2, 0} c_{f_0' a_2} e^{i\varphi_{f_0' a_2}} \Delta_{f_0'}(m_{\eta\eta}) \Delta_{a_2}^*(m_k) P_2^0(\theta_k, \phi_k) \\
& + \sum_{k=1,2} a_{f_0'} a_{a_2'} c_{f_0' a_2'} e^{i\varphi_{f_0' a_2'}} \Delta_{f_0'}(m_{\eta\eta}) \Delta_{a_2'}^*(m_k) P_2^0(\theta_k, \phi_k) \\
& + \sum_{k=1,2} a_{f_0} a_{a_2'} c_{f_0 a_2'} e^{i\varphi_{f_0 a_2'}} \Delta_{f_0}(m_{\eta\eta}) \Delta_{a_2'}^*(m_k) P_2^0(\theta_k, \phi_k) \\
& + \sum_{k=1,2} a_{f_0'} a_{a_2'} c_{f_0' a_2'} e^{i\varphi_{f_0' a_2'}} \Delta_{f_0'}(m_{\eta\eta}) \Delta_{a_2'}^*(m_k) P_2^0(\theta_k, \phi_k)
\end{aligned}$$

The weight function uses the amplitudes of the simplified canonical formulation. The fitted hypothesis assumes the isoscalar resonances $f_0(975)$, $f_0'(1500)$ and $f_2'(2135)$ (first row in the formula) and the isovectors $a_0(980)$ (second row), $a_2(1320)$ (fourth and fifth row) and $a_2'(1650)$ (third row) (see chap. 4.2., figure 4.11). Also taken into account are the interferences between a_0 and a_2 (sixth row), a_0 and f_2' (seventh row), f_0 and a_2 (eighth row), f_0' and a_2 (ninth row), f_0' and a_2' (tenth row) and a_2 and a_2' (eleventh row). Additionally the interferences of the crossing a_0 bands in the Dalitz plot (third expression on the second row) and the crossing a_2 bands (fifth row) are fitted. The free parameters of the fit are the couplings a , the strengths of interferences c , the relative phases φ and the masses and width of the resonances, which are implicitly contained in the dynamical functions Δ .

Bibliography

- [1] L. Montanet et al., *Review of Particle Properties*, Phys.Rev. **D50**(1994)2392
- [2] S. Spanier, Ph.D. thesis, University Mainz, 1994
- [3] A. Hasan et al., Proceedings of the Low Energy Antiproton Konferenz, 1994
- [4] G. Folger, *Offline Reconstruction Software*, CB-note 93(1989), unpublished
- [5] C.A. Meyer, *Chamber Reconstruction Software, LOCATER*, CB-note 93(1990), unpublished
- [6] F.H. Heinsius und Th. Kiel, *Crystal Reconstruction Software*, CB-note 92(1990), unpublished
- [7] M. Burchell, *Global Tracking Particle Bank Structure*, CB-note (1991), unpublished
- [8] T. Degener, M. Kunze, J. Lüdemann und K. Peters, *Object-Oriented Offline Analysis for C++ Programmers, CBoff++*, unpublished
- [9] P. Schmidt, *PED-Energy Correction Function for inflight Data*, CB-note 161a(1994), unpublished
- [10] K. Peters, *The Monte Carlo Programmer's Guide for CB*, CB-note 96(1990), unpublished
- [11] R. Glantz, *Untersuchungen zur Richtungsrekonstruktion für Photonen im Crystal-Barrel-Kalorimeter*, Diplomarbeit, University Hamburg, 1992, unpublished
- [12] R. Brun et al., *GEANT 3 User's Guide*, CERN DD/EE/84-1, rev. 1987
- [13] C. Amsler, *Vertex from neutral events*, CB-note 15(1985)
- [14] D.V. Bugg, *Formulae used to fit antiproton proton goes to $3\pi^0\eta$ in flight*, CB-note 273(1995), unpublished
- [15] K. Beuchert, Ph.D. thesis, Ruhr-Universität Bochum, 1995
K. Beuchert et al., Proceedings of the Nucleon-Antinucleon Conference, NAN'95, Moscow, 1995
- [16] W. Weise, Proceedings of the Low Energy Antiproton Physics Conference, LEAP'92, Courmayeur, 1992
- [17] J.M. Blatt and V. Weisskopf, *Theoretical Nuclear Physics*, Wiley, New York, 1952
F. v.Hippel and C. Quigg, Phys.Rev.**D5**(1988)563
- [18] K. Peters, private communications
K. Peters and E. Klempt, *The suppression of $s\bar{s}$ pair creation from tensor meson decays*, Phyl.Lett. **B352**(1995)467
- [19] D.V. Bugg, private communications
- [20] S.U. Chung, *$3\pi^0$ in flight*, unpublished
- [21] S.U. Chung, *Spin Formalisms*, CERN 71-8 (1971)
- [22] A. Messiah, *Quantenmechanik*, Vol.2, Walter de Gruyter, Berlin, 1985
- [23] K. Königsmann, , CB-note 195, unpublished
- [24] F. James and M. Roos, *MINUIT, Function Minimization and Error Analysis*, CERN DD D506, 1987